Nonlinear Multibody Modelling of Flexible Aircraft with Flared Hinged Wing Tips

Kelvin Chi-Wing Cheng[†], Alvaro Cea[‡], and Rafael Palacios[§].
Department of Aeronautics, Imperial College London, SW7 2AZ, United Kingdom

Andrea Castrichini[¶], Thomas Wilson[‖].
Airbus Operations, Ltd., BS99 7AR, United Kingdom

A nonlinear simulation strategy is presented for low-speed flexible aircraft with flared hinged wings. A multibody solver based on geometrically-exact composite beams is coupled with unsteady vortex lattice aerodynamics in time domain. The structural model is first verified against simulations on a flexible double pendulum at various stiffness and hinge orientations. Aeroelastic simulations of a flexible wing with flared hinged wing tips are then conducted, and compared against previous experimental and numerical results. Finally, a full-vehicle configuration featuring flared hinged wing tips is introduced, based on a high-altitude long-endurance T-tail aircraft. Aeroelastic trim and equilibrium states are computed for both the original vehicle and the modified aircraft with hinged wing tips, for the analysis of 1g plus gust responses in the vertical and lateral directions. Results shed light on the coupled nonlinear aeroelastics and flight dynamics exhibited by various configurations of varying mass and stiffness definitions in gust encounters. It is found that the response of the aircraft with flared hinged wing tips considering geometrical nonlinearities is predominantly bounded by that of cases with extended and upturned wing tips, with nonlinear trends in flare angle, gust lengths and intensities uncovered and weighed in their contributions to the overall flexible aircraft dynamics.

Presented as Paper 2024-1441 at the AIAA SCITECH 2024 Forum, Orlando, FL, 8-12 January, 2024
[†]PhD Student, CAGB 308, South Kensington Campus. (kelvin.cheng@imperial.ac.uk)
[‡]Research Associate, CAGB 308, South Kensington Campus. (alvaro.cea-esteban15@imperial.ac.uk)
[§]Professor in Computational Aeroelasticity, CAGB 310, South Kensington Campus. AIAA Associate Fellow (r.palacios@imperial.ac.uk)
[¶]Senior Future Projects Engineer, Airbus Operations, Ltd., Filton. (andrea.a.castrichini@airbus.com)
[‖]Senior Expert for Aeroelasticity, Airbus Operations, Ltd., Filton. (thomas.wilson@airbus.com)

I. Introduction

The net zero target by 2050 in aviation calls for disruptive thinking at the systems level, and a renewed demand for technologies that offer significant improvements in fuel efficiency. [1] One of the main avenues to achieve cuts in emissions is the development of weight-saving technologies in aircraft design. It is commonly accepted that with the current architecture of wing design, in the absence of a paradigm shift in technologies deployed, by fine-tuning the global aero-structural design of current wings only single digit weight savings can be achieved [2]. One of those more mature (on the TRL scale) next-generation technologies from biomimicry is a morphing aerostructure for active load alleviation [3], which despite the complexities in implementation and failure modes remains promising [4]. Another example would be the use of flared hinged wings [5, 6], in particular ones that allow for free-flapping motion inflight akin to that of birds, to exploit the potential gust load alleviation and maneuvering advantages, while remaining locked: extended at 0° about the hinge line relative to the wing for cruise, and upwards at 90° for taxiing, the latter to comply with gate restrictions. Arguably the most important feature of the hinge is the flare angle - this describes how the hinge axis is oriented with regards to the freestream direction. A hinge axis pointing towards the centerline downstream (positive flare angle) produces a restoring moment by the change of angle of incidence due to rotation of the wing tips when perturbed in either direction from trim, ensuring that the mechanism is statically stable.

Previous studies have demonstrated that flared hinged wings can provide both static and dynamic load alleviation; where the static load alleviation is mostly a function of the (positive) flare angle, and the dynamic load alleviation in a vertical 1-cos gust response is improved with flare, reduced wingtip mass, and increased hinge flexibility [7]. Subsequent static analyses in rectilinear flight have shown that, at higher angles of attack, the wingtip equilibrium angle is driven by the geometric nonlinearities, as well as the fact that sideslip angle changes the effective flare angle of the hinges [8]. Dynamic studies have also shown that load alleviation with hinged configuration appears both under vertical and lateral gusts, and that the effects of nonlinearities seen in the wingtip response do not readily translate to the main airframe [9]. Separately the observation that a lighter wing tip would react faster to the incoming vertical gust, and provide more significant load alleviation of the first positive peak load (whilst worsening the first negative peak load, and introducing extra oscillations with the wingtip flapping) is verified experimentally and numerically in [10]. A prior independent experimental campaign confirms the relative alleviation / worsening of the first positive and negative peaks and subsequent transient oscillations of wing tip and associated loads, and also provides the sensitivity with regards to the gust length [11]. Major mechanisms of the geometric nonlinearities are identified and discussed, in the context of an experimental-numerical comparison in [12], and have also established that sideslip has little impact on the nonlinear load alleviation properties of the wing tip without rigid-body modes [13].

Much work has been done in both the modelling and experimentation aspects of the problem and computational results have largely established the quasi-steady aeroelastic performance of flared hinged wings. Recent advances have been made in multiple directions, assessing the viability of such a wingtip device, all converging to the eventual goal of realising the concept in a commercial transport aircraft - these include a better understanding of the impact of wing stiffness and release timing [14] on the load-alleviating properties of the mechanism, the stability boundary as a function of an additional trim device on the wing tip, model parameters, and types of nonlinearities involved [15], the folding wing tips featuring in a scaled wind tunnel model aircraft with high aspect ratio wings [16], the extrapolation of wind tunnel results to a full-size model via scaling methods [17], the improvements on roll performance by reducing the roll damping and increasing the peak acceleration achieved seen on a scaled model in wind tunnel tests and associated numerical modelling [18], and the assessment of varying degrees of roll maneuverability by control surface location and dynamic pressure in the transonic regime [19].

In terms of the numerical modelling techniques employed, some developments have been necessary in structure and aerodynamic methods. A number of structural studies have used modal-superposition based methods [7, 10, 11, 14], to enable simulations using MSC NASTRAN. The flared hinged wing tips often introduce geometric nonlinearities, and formulations have been derived based on the equations of motion for a rigid flared hinged wing tip attached to the (linear) inner wing [8, 9, 13, 15, 18]. Another class of methods obtain linearised models about the nonlinear equilibrium by iterations of corrected follower-force aeroelastic simulation [12]. To fully capture the geometrical nonlinearities, a nonlinear strain-based geometrically exact beam formulation was used in [19] for coupled flexible inner wing and wing tips. As for the aerodynamic modelling, most previous studies utilised doublet lattice methods (DLM), both in the canonical form [7, 10, 14], and in the augmented form where corrections are applied to approximate follower aerodynamic forces, by applying a cosine relationship between inner wing and wing tips in the generalised aerodynamic coefficients matrix [8] for quasi-steady results, later extended to unsteady cases [9]. Follower-force aerodynamic models are also obtained through an iterative FSI process as described above in [12]. Other studies have leveraged different aerodynamic models in strategy and fidelity: 1D calculation of lift from a defined polar allows for easy corrections for geometric nonlinearities [11], which readily extends to modified strip theory in 2D [18], on top of which aerodynamic nonlinearities can be considered [15]. The vortex lattice method (VLM) was implemented in [13] which lends itself to a native description of the deflected panel geometry. Finally, method of segments leveraging steady CFD solutions of the full model has been developed in [19]. They build cross-sectional surrogate models from the CFD results to capture quasi-steady transonic aerodynamic

nonlinearities.

To profile the transient response of the wing assembly with the hinge mechanism it is essential that the nonlinear effects of large displacements and rotations are incorporated, both in the main, usually flexible wing, as well as the wing tips, which can assume a wide range of configurations depending on dynamical conditions. It is often computationally prohibitive to perform trade studies on the aeroelastic wing assembly with high fidelity tools. Therefore, a multibody solver has been developed in SHARPy [20], an open-source, nonlinear aeroelastic simulation toolbox that couples aerodynamics obtained with the unsteady vortex lattice method (UVLM) with a structural description given by a nonlinear displacement-based geometrically-exact composite beam model (GEBM). This work presents a general multibody solution compatible to both the UVLM and the GEBM. Such an approach often needs of special numerical schemes, since the rigid-body motions and elastic deformations can exhibit very different time scales [21, 22]. Among the methods for solving flexible multibody dynamics, as reviewed in [23], two formulations stands out for applications with large displacements: geometrically exact approaches and the Absolute Nodal Coordinate (ANC) formulation. The former is implemented in this work using displacements and rotations as primary variables and more details are given below. The latter has been developed by approximating the displacement spatial field as polynomials [24], and directly applying the equations of solid mechanics to the resulting ad-hoc displacement field. The two formulations have been compared in [25], with the outcome that geometrically-exact formulations are more involved in terms of implementation and mathematical modelling, but offer an edge in computational speeds and accuracy.

In this work, we will develop, verify, and examine the capabilities of the nonlinear aeroelastic multibody formulation with test cases, including a flared double pendulum, and a demonstrative model of an aeroelastic wing tip on a flexible main wing, as precursors to the aeroelastic simulation of a multibody high altitude long endurance (HALE) aircraft. The HALE configuration is chosen for its demonstrated [26] strong nonlinearities with a simple yet representative layout - it is hoped that this will provide the community with a highly reproducible set of results for future validation of nonlinear aeroelastic frameworks for aircraft with flared hinged wings. With that we will demonstrate the robustness of the solution procedure with coupled flight dynamics and aeroelastics, and shed light on 1) the extent of the static (at trim) and dynamic load alleviation in vertical gust affected by gust length and intensity, flare angle, wingtip mass, and stiffness; 2) the dynamic load alleviation in lateral gusts as a function of the flare angle; 3) comparison of the above with the extended and upturned wing tip configurations; and 4) whether the presence of the hinge would promote favourable system characteristics like increased damping for transient loads, improved handling characteristics, etc.

The structure of the rest of this paper goes as follows. In Section II, we will delve into the theoretical background and set-up of the nonlinear multibody time-domain simulation environment for free-flying flexible aircraft used in this work. In Section IV, we will verify the flexible multibody solution with rigid and flexible comparisons for a double pendulum with different flare angles to demonstrate the accuracy of the formulation. In Section III, we will perform aeroelastic simulations on two separate models - the first a wing assembly with flared hinged tips published in literature, for cross-validation of results; the second a parametrised full HALE aircraft model flying through vertical and lateral gust profiles, to establish the robustness of the solution procedure, and uncover insights on the coupled flight dynamics and aeroelastics of the system.

II. Theory and Implementation

A. Nonlinear aeroelastic simulation environment

This section outlines the theory and implementation of the simulation environment for flexible aircraft dynamics, in particular, the extension of the basic approach of Ref. [27] to describe problems with flexible multibody dynamics.

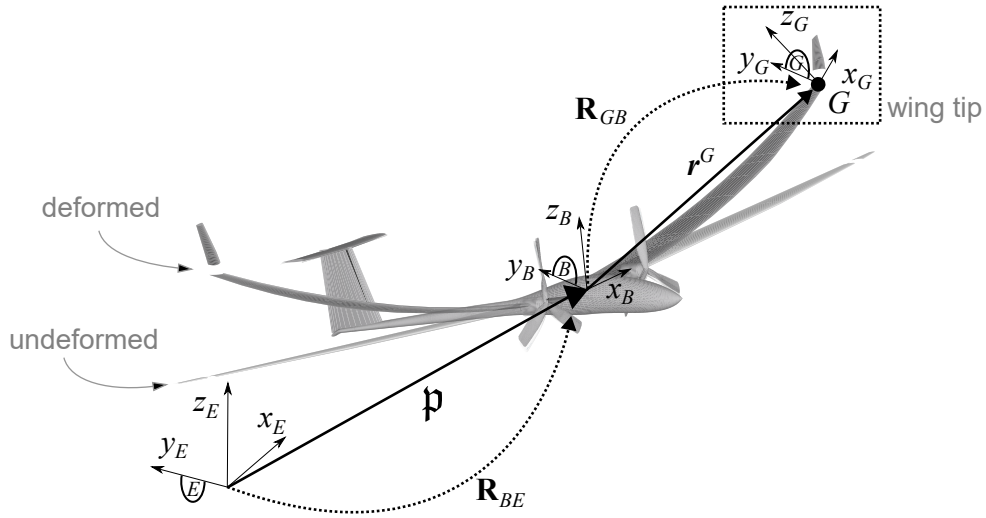
1. Definition of reference frames and kinematics

Figure 1 defines the notation, used to describe the kinematics of the flexible wing with hinged wing tips. We begin from the Earth frame E in Figure 1a, from which we define $\mathfrak{p}(t)$ as the time-varying vector to the body-attached frame B used to track the vehicle and define its absolute orientation. In this paper the right-handed B frame is at the root of the wing, with positive x direction towards the right wing, and positive z direction upwards. The rotation matrix from E to B frame $\mathbf{R}_{BE}$ is defined with a choice of parametrisation, in this case the quaternion χ^B, for the generality of the description. In the B frame we define $\boldsymbol{r}_B^G$ as the vector to the material frame at the tip of the main wing, frame G. The rotation matrix from B to G frame $\mathbf{R}_{GB}$ is defined, again with a choice of parametrisation, in this case the Cartesian Rotation Vector (CRV) $\boldsymbol{\psi}_B^G$, for CRVs only uses three degrees of freedom (DoFs) which corresponds to the usual linear rotations for infinitesimal rotations.

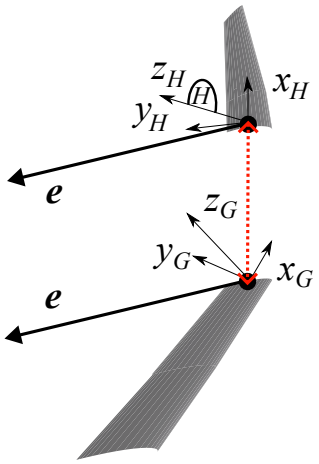
On the wing tip itself in Figure 1b, separated by the hinge, we define the body-attached frame H at its root where the rotation matrix from the global frame $\mathbf{R}_{HE}$ is a function of the quaternion χ^H, without loss of generality, and for ease of expressing common quantities in the Earth frame in the later sections. Inertial velocities of body-fixed frames, i.e., B and H, are given in their own frames of reference (FoRs) respectively by $\boldsymbol{v}_B^B$, $\boldsymbol{\omega}_B^B$ and $\boldsymbol{v}_H^H$, $\boldsymbol{\omega}_H^H$, where those at material frames, i.e. G, require a more involved formulation described in Section II.A.3.

As the aeroelastic wing with the hinged wing tips undergoes displacements and rotations, the hinge line

vector $\boldsymbol{e}$ in any arbitrary direction (but usually lying on the chordwise-spanwise plane of the wing in the material frame, for continuity across the hinge) as visualised, is a function of rigid body translational and rotational movements, and flexible deformations, and almost always a function of time. Defining instead the projections of the hinge line vector in the two local frames of reference gives $\boldsymbol{e}_H = \mathbf{R}_{HB}\boldsymbol{e}_B$, such that these vectors are now constant in time, from Euler's rotation theorem (Chapter 4.3.2 of Ref. [27]).



(a) Frames and notations for aircraft with flared hinged wings



(b) Inset showing frames and notations of the wing tip

Fig. 1 Labelled quantities and frames of the flexible multibody wing assembly

2. Flexible Multibody Formulation with Lagrange Multipliers

To obtain the overall structural system of equations we assemble the relevant equation of motion for each generalised DoF $\mathbf{x}$, consisting, for each of the beams within the multibody structure, the global attitude, rigid

body velocities, and the flexible deformations described by displacements and rotations at the grid nodes of the beam elements, which is consistent in nomenclature as in Equation 9.4 in [27]. The constraints are then appended as functions of one or several of the DoFs in the formulation. To represent the connections between different nodal DoFs and/or to address the fact that we have not explicitly chosen the DoFs to be linearly independent, we introduce extra constraint equations $\boldsymbol{g}$ which are itemised in Section II.A.3. Multiplying with Lagrange multipliers defines an augmented Lagrangian for the system, from which we arrive at the general form of the multibody problem as

$$\begin{cases} \mathbf{M}(\mathbf{x})\ddot{\mathbf{x}} + \mathbf{B}^{\top}(\mathbf{x}, \dot{\mathbf{x}}, t)\boldsymbol{\lambda} = \mathfrak{f}(\mathbf{x}, \dot{\mathbf{x}}, t) = \mathfrak{f}_{ext}(\mathbf{x}, \dot{\mathbf{x}}) - \mathfrak{f}_{gyr}(\mathbf{x}, \dot{\mathbf{x}}) - \mathfrak{f}_{stif}(\mathbf{x}), \\ \boldsymbol{g}(\mathbf{x}, \dot{\mathbf{x}}, t) = \mathbf{B}(\mathbf{x}, \dot{\mathbf{x}}, t)\dot{\mathbf{x}} + \boldsymbol{g}_0 = 0 \end{cases} \tag{1}$$

in which $\mathbf{M}$ is the mass matrix and $\mathfrak{f}$ includes the external, gyroscopic, and stiffness forces respectively, and $\mathbf{B} = \frac{\partial \boldsymbol{g}}{\partial \dot{\mathbf{x}}}$ is the Jacobian of the constraints [28]. In the problems of interest, specifically with flexible hinged wing tips, $\mathfrak{f}_{ext}$ is given by a co-simulation with a UVLM solver [20][29] to give the aerodynamic forcing $\mathfrak{f}_{aero}$. If we then write Equation (1) in incremental form and recast we obtain

$$\begin{bmatrix} \mathbf{M} & 0 \\ 0 & 0 \end{bmatrix} \begin{pmatrix} \Delta\ddot{\mathbf{x}} \\ \Delta\dot{\boldsymbol{\lambda}} \end{pmatrix} + \begin{bmatrix} \mathbf{C} & \mathbf{B}^{\top} \\ \mathbf{B} & 0 \end{bmatrix} \begin{pmatrix} \Delta\dot{\mathbf{x}} \\ \Delta\boldsymbol{\lambda} \end{pmatrix} + \begin{bmatrix} \mathbf{K} & 0 \\ 0 & 0 \end{bmatrix} \begin{pmatrix} \Delta\mathbf{x} \\ 0 \end{pmatrix} = \begin{pmatrix} \mathfrak{r}^{\circ} \\ -\boldsymbol{g}^{\circ} \end{pmatrix} + \text{H.O.T.} \tag{2}$$

where the tangent damping and stiffness matrices $\mathbf{C}$ and $\mathbf{K}$, as well as the residual vector $\mathfrak{r}^{\circ}$ are given as

$$\begin{cases} \mathbf{C} = \underbrace{\dfrac{\partial \mathbf{B}^{\top}\boldsymbol{\lambda}}{\partial \dot{\mathbf{x}}}}_{\overline{\mathbf{C}}} - \dfrac{\partial \mathfrak{f}}{\partial \dot{\mathbf{x}}}, \\ \mathbf{K} = \dfrac{\partial (\mathbf{M}\ddot{\mathbf{x}})}{\partial \mathbf{x}} + \underbrace{\dfrac{\partial \mathbf{B}^{\top}\boldsymbol{\lambda}}{\partial \mathbf{x}}}_{\overline{\mathbf{K}}} - \dfrac{\partial \mathfrak{f}}{\partial \mathbf{x}}, \\ \mathfrak{r}^{\circ} = \mathfrak{f} - \mathbf{M}\ddot{\mathbf{x}} - \mathbf{B}^{\top}\boldsymbol{\lambda} \end{cases} \tag{3}$$

evaluated at the reference point. We determine $\mathbf{B}$ for the common lower pair joints that we are interested in, then, reminding ourselves of the Newmark-β formulation for a generalised state variable $\boldsymbol{q}$,

$$\begin{cases} \boldsymbol{q}_{n+1} = \boldsymbol{q}_n + \dot{\boldsymbol{q}}_n \Delta t + (\frac{1}{2} - \beta_T)\ddot{\boldsymbol{q}}_n \Delta t^2 + \beta_T \ddot{\boldsymbol{q}}_{n+1} \Delta t^2 + \mathcal{O}(\Delta t^3), \\ \dot{\boldsymbol{q}}_{n+1} = \dot{\boldsymbol{q}}_n + (1 - \gamma_T)\ddot{\boldsymbol{q}} \Delta t_n + \gamma_T \ddot{\boldsymbol{q}}_{n+1} \Delta t^2 + \mathcal{O}(\Delta t^3). \end{cases} \tag{4}$$

Equations (2) and (4) define a well-posed linear problem, which is used to iteratively update the nonlinear equations in (1), using a predictor-corrector algorithm to accelerate convergence. A verification study on a flexible pendulum is included in the appendix. For aeroelastic problems, the nodal displacements are used

to deform the lifting surfaces on which the aerodynamics solver computes nodal loads [30], which is in turn passed onto the multibody solver for the next time step in a classical FSI coupling scheme.

As mentioned above, the unsteady aerodynamics are modelled by the UVLM. This approach easily accommodates the wingtip kinematics. The UVLM grid boundary at the hinge is skewed by the hinge axis along the flare angle, as shown in Figure 2. This ensures as the structure rotates about the hinge axis there is no ambiguity of the aero-structural force-displacement interface, as discussed in Ref. [31]. Here, all UVLM grid nodes along the same chord-wise line are controlled by the displacements and rotations of the corresponding beam node. The careful choice of span-wise discretisation is hence crucial to avoid a self-intersecting UVLM grid.

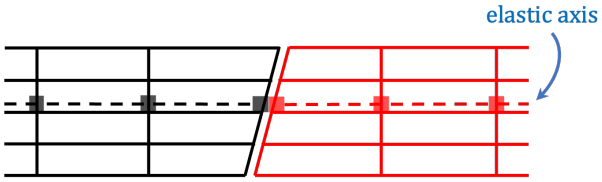


Fig. 2 UVLM grid boundaries with beam nodes near the hinge

3. Multibody constraints for the hinged wing tip

Equation (1) describes the coupling of a generic flexible multibody structure; this formulation has been applied previously on other multibody systems such as wind turbines [32]. For a hinge connection between 2 beams, we require three and two equations for the linear and angular velocities respectively to allow only for one degree of freedom, which is the rotation about the hinge axis. They are derived next.

Linear velocity constraint We begin by placing the condition of same linear velocity at frames G and H. Equating the velocities across the connection, in H frame gives

$$\boldsymbol{v}_H^H = \mathbf{R}_{HB}\left(\dot{\boldsymbol{r}}_B^G + \boldsymbol{v}_B^B + \widetilde{\boldsymbol{\omega}}_B^B \boldsymbol{r}_B^G\right), \tag{5}$$

which when written as a constraint in matrix form in the inertial frame E, and following the notation in Equation (1), is

$$\boldsymbol{g}_1 = \begin{bmatrix} -\mathbf{R}_{EB}(\chi^B) & -\mathbf{R}_{EB}(\chi^B) & \mathbf{R}_{EB}(\chi^B)\widetilde{\boldsymbol{r}}_B^G & \mathbf{R}_{EH}(\chi^H) \end{bmatrix} \begin{bmatrix} \dot{\boldsymbol{r}}_B^G \\ \boldsymbol{v}_B^B \\ \boldsymbol{\omega}_B^B \\ \boldsymbol{v}_H^H \end{bmatrix} = \mathbf{B}_1(\dot{\mathbf{x}}, \mathbf{x}, t)\dot{\mathbf{x}} = 0, \tag{6}$$

where in these expressions $\widetilde{\bullet}$ or $skew(\bullet)$ is the cross product operator. Apart from introducing the constraint as an extra equation in the system, we would also have to update the residual $\mathfrak{r}^\circ$, and evaluate $\overline{\mathbf{C}}$ in Equation (3). The only non-zero terms in the full-rank matrix $\overline{\mathbf{C}}$ are the submatrices

$$\begin{aligned} \overline{\mathbf{C}}_{\dot{\boldsymbol{r}}_B^G, \chi^B} &= -\frac{\partial}{\partial \chi^B}\left((\mathbf{R}_{EB}(\chi^B))^\top \boldsymbol{\lambda}\right), \\ \overline{\mathbf{C}}_{\boldsymbol{v}_B^B, \chi^B} &= -\frac{\partial}{\partial \chi^B}\left((\mathbf{R}_{EB}(\chi^B))^\top \boldsymbol{\lambda}\right), \\ \overline{\mathbf{C}}_{\boldsymbol{\omega}_B^B, \chi^B} &= \frac{\partial}{\partial \chi^B}\left((\mathbf{R}_{EB}(\chi^B))^\top \left(\widetilde{\boldsymbol{r}}_B^G \boldsymbol{\lambda}\right)\right), \\ \overline{\mathbf{C}}_{\boldsymbol{v}_H^H, \chi^H} &= \frac{\partial}{\partial \chi^H}\left((\mathbf{R}_{EB}(\chi^H))^\top \boldsymbol{\lambda}\right). \end{aligned} \tag{7}$$

Likewise the only non-zero contribution to the full-rank matrix $\overline{\mathbf{K}}$ is the submatrix

$$\overline{\mathbf{K}}_{\boldsymbol{\omega}_B^B, \boldsymbol{r}_B^G} = -\mathbf{R}_{EB}(\chi^B)\widetilde{\boldsymbol{\lambda}}. \tag{8}$$

Angular velocity constraint To apply the angular velocity constraint, in practice we restrict any two pairs of corresponding points on the vectors to always have the same linear velocity. Choosing the origins of the vectors in Figure 1b as the first pair gives Equation (5), and additionally choosing two points along the vectors give their common linear velocity in the H frame as

$$\boldsymbol{v}_H^H + \widetilde{\boldsymbol{\omega}}_H^H \boldsymbol{e}_H = \mathbf{R}_{HB}\left(\dot{\boldsymbol{r}}_B^G + \boldsymbol{v}_B^B + \widetilde{\boldsymbol{\omega}}_B^B \boldsymbol{r}_B^G\right) + \mathbf{R}_{HG}(\text{skew}(\mathbf{T}^{GB}\dot{\boldsymbol{\psi}}_B^G + \mathbf{R}_{GB}\boldsymbol{\omega}_B^B)\boldsymbol{e}_B), \tag{9}$$

where $\mathbf{T}$ is the tangential rotational operator described in Appendix C of [27], from which Equation (5) is eliminated to give

$$\widetilde{\boldsymbol{\omega}}_H^H \boldsymbol{e}_H = \mathbf{R}_{HG}(\text{skew}(\mathbf{T}^{GB}\dot{\boldsymbol{\psi}}_B^G + \mathbf{R}_{GB}\boldsymbol{\omega}_B^B)\boldsymbol{e}_B), \tag{10}$$

which is transformed to G frame and recast in matrix form as

$$\boldsymbol{g}_2 = \begin{bmatrix} \widetilde{\boldsymbol{e}}_B \mathbf{R}_{GB}(\boldsymbol{\psi}_B^G) & \widetilde{\boldsymbol{e}}_B \mathbf{T}^{GB}(\boldsymbol{\psi}_B^G) & -\mathbf{R}_{GB}(\boldsymbol{\psi}_B^G)\mathbf{R}_{BE}(\chi^B)\mathbf{R}_{EH}(\chi^H)\widetilde{\boldsymbol{e}}_H \end{bmatrix} \begin{bmatrix} \boldsymbol{\omega}_B^B \\ \dot{\boldsymbol{\psi}}_B^G \\ \boldsymbol{\omega}_H^H \end{bmatrix} = \mathbf{B}_2(\dot{\mathbf{x}}, \mathbf{x}, t)\dot{\mathbf{x}} = 0. \quad (11)$$

We then follow a similar procedure as in Section II.A.3 to obtain $\overline{\mathbf{C}}$ and $\overline{\mathbf{K}}$,

$$\begin{aligned}
\overline{\mathbf{K}}_{\boldsymbol{\omega}_B^B, \boldsymbol{\psi}_B^G} &= -\frac{\partial(\mathbf{R}_{GB}(\boldsymbol{\psi}_B^G))^\top}{\partial \boldsymbol{\psi}_B^G}(\widetilde{\boldsymbol{e}}_B \boldsymbol{\lambda}), \\
\overline{\mathbf{K}}_{\dot{\boldsymbol{\psi}}_B^G, \boldsymbol{\psi}_B^G} &= -\frac{\partial(\mathbf{T}(\boldsymbol{\psi}_B^G))^\top}{\partial \boldsymbol{\psi}_B^G}(\widetilde{\boldsymbol{e}}_B \boldsymbol{\lambda}), \\
\overline{\mathbf{K}}_{\boldsymbol{\omega}_H^H, \boldsymbol{\psi}_B^G} &= \widetilde{\boldsymbol{e}}_H \mathbf{R}_{HE}(\chi^H)\mathbf{R}_{EB}(\chi^B)\frac{\partial(\mathbf{R}_{BG}(\boldsymbol{\psi}_B^G))}{\partial \boldsymbol{\psi}_B^G}\boldsymbol{\lambda}, \\
\overline{\mathbf{C}}_{\boldsymbol{\omega}_H^H, \chi^B} &= \widetilde{\boldsymbol{e}}_H \mathbf{R}_{HE}(\chi^H)\frac{\partial \mathbf{R}_{EB}(\chi^B)}{\partial \chi^B}(\mathbf{R}_{BG}(\boldsymbol{\psi}_B^G)\boldsymbol{\lambda}), \\
\overline{\mathbf{C}}_{\boldsymbol{\omega}_H^H, \chi^H} &= \widetilde{\boldsymbol{e}}_H \frac{\partial \mathbf{R}_{HE}(\chi^H)}{\partial \chi^H}(\mathbf{R}_{EB}(\chi^B)\mathbf{R}_{BG}(\boldsymbol{\psi}_B^G)\boldsymbol{\lambda}).
\end{aligned} \quad (12)$$

The formulation above can be further simplified with alternative choices for the rotation parametrisation - in particular, one could consider $\mathbf{R}_{GH}$ with a 1D dependency in the fold angle, for the third term in $\mathbf{B}_{n2}$. Here, we opted to express equivalence in the body-attached frame both to accommodate the existing solver structure and to keep the formulation general for future additional kinematic constraints.

4. Trimming procedure

In general, in a nonlinear trim routine, a flexible aircraft is trimmed by subsequent static computations of deformed geometry and load subjected to control inputs, which are given by a gradient based method as a function of previous total forces and moments on the system. Loosely speaking, when dealing with the relatively simple case of longitudinal trim, we can associate a few first-order input/output systems by physical arguments - that lift is mostly influenced by angle of attack, drag by thrust, and pitching moment by elevator deflection.

For a flexible aircraft with flared hinged wing, the hinge mechanism often results in nonconvergence, or at best, poor convergence, using the static equilibrium approach, and an alternative method is required to obtain dynamic equilibria of the multibody system at a lower computational cost than an unconstrained dynamic simulation. We have built a trim algorithm for this work that has architecture borrowed from a simple flight control system. In particular, by replacing the gradient based approach with independent

single-input single-output (SISO) control systems loosely coupled by the nonlinear aeroelastic dynamics, we provide the multibody system with natural damping to promote convergence when time-stepping the solution. In the case of longitudinal trim, we have clamped the otherwise free-flying aircraft except the pitching degree of freedom (as it is the only necessary DoF), and set up 3 PI controllers for lift-angle of attack, drag-thrust, pitching moment-elevator relationships, for zero targets, for all measured forces and moments, as will be shown in Section III.B.2.

III. Aeroelastic Results

A. Aeroelastic multibody wing assembly

The first test case is a flexible full wing with flared hinged wing tips. It is set up with similar structural complexity as the flared double pendulum model in Appendix IV. Experimental and numerical results are those of [12], [15], and [11]. To capture the main viscous aerodynamic effects we apply sectional corrections as detailed in [29, 30] based on the lift and drag polars for the NACA0015 airfoil at $\mathrm{Re} = 200000$. Selected properties of the wing assembly as well as simulation inputs are presented in Table 1. Figure 3 shows the single tracked variable (symmetric across the global x axis) as the fold angle θ - with the three coloured regions with varied stiffness and crosses denoting lumped masses and inertias, as per the structural layout of the numerical model described in [12].

Table 1 Key Parameters for flexible slender prismatic wing with wing tip

Parameters	Values	Units
Air density	1.225	$\mathrm{kg/m^3}$
Half-span	1.0	m
Wingtip span	0.345	m
Chord	0.15	m
Flare angle β	10	deg
Angle of attack	2.5, 5.0, 7.5, 10.0	deg
Freestream velocity	12 to 28 (in 2 increments)	$\mathrm{m\ s^{-1}}$
Gravity	9.81	$\mathrm{m\ s^{-2}}$

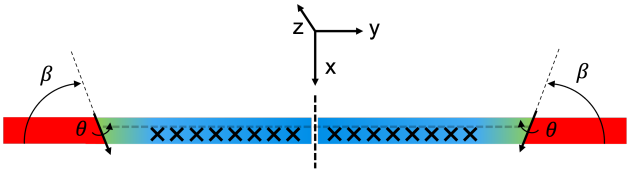


Fig. 3 Wing assembly with flared hinged wing tips

Referring to Figure 4, the numerical model [12] is an iterative aeroelastic solution process partly leveraging NASTRAN routines to model follower aerodynamic loads on the deformed structure, solving for, and at the converged fold angle for each input condition. The secondary effects of inner-wing flexibility, and local changes in AoA and sideslip due to the flare angle are not considered. At certain angle of attack and velocity combinations in the time-domain SHARPy multibody aeroelastic simulations there exist stable dynamic equilibrium fold angles - those are denoted with triangles. Where a particular combination of input conditions give limit cycle oscillations, the mean fold angle is calculated as the average of the maximum and minimum fold angles seen in the time histories of the sustained LCO - those are denoted with asterisks.

At lower angles of attack, SHARPy predicts the experimental data points similarly to the model in [12]. In this case, the nonlinearities present in the aeroelastic modelling are relatively small. At higher angles of attack we see a slightly better alignment with experimental results versus [12] towards higher velocities - where the large main wing deformations start to influence and interact with the wingtip dynamics, and its effect captured by the nonlinear coupled model in SHARPy natively. The experimental flutter boundary of this wing assembly as quoted in [12] is indicated in Figure 4, which is just beyond all available quoted experimental data points in circles. The SHARPy stability boundary can be estimated from time-domain simulation and compares well with the experiments.

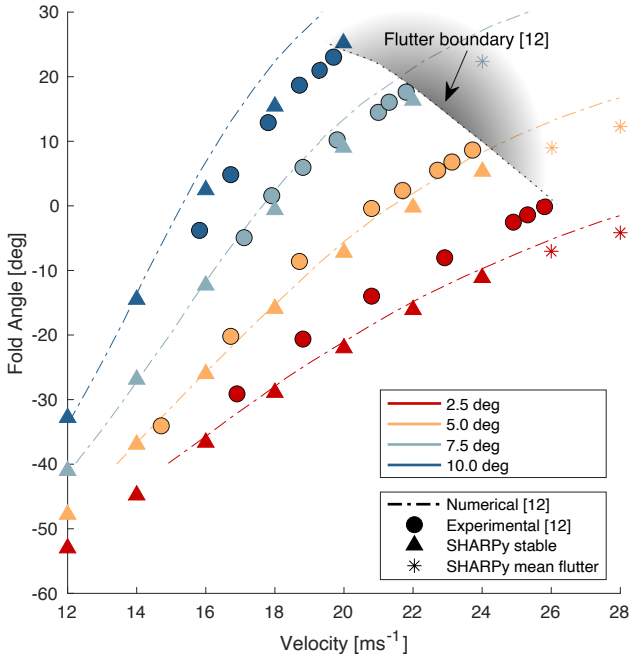


Fig. 4 SHARPy equilibrium and mean LCO fold angle θ for various velocity and angle of attack combinations, overlaid on numerical and experimental data from [12]

At $\alpha = 2.5°$ and $u_\infty = 26.8ms^{-1}$ we compare LCO response of the wing assembly at the same flare angle of $\beta = 10°$. Here, a different numerical aeroelastic model is used [15] coupling unsteady strip theory with an Euler-Bernoulli beam with a rigid wingtip attachment (the structural solver does not model the hinge flare angle, i.e. the wingtip is along a perpendicular hinge line against the spanwise direction). Broadly speaking the response predictions are good by both formulations - the slight differences in the prediction are thought to be due to the secondary effects by the flare angle on the geometrical nonlinearities, and the differences in spanwise distribution of lift and stall from the aerodynamic nonlinearities. The initiation of the dynamic response into a fully developed LCO is different in each of the setup and can be seen in Figure 5.

We have established the multibody aeroelastic formulation as implemented in SHARPy produces results that largely confirms existing knowledge on a representative flared hinged wing assembly.

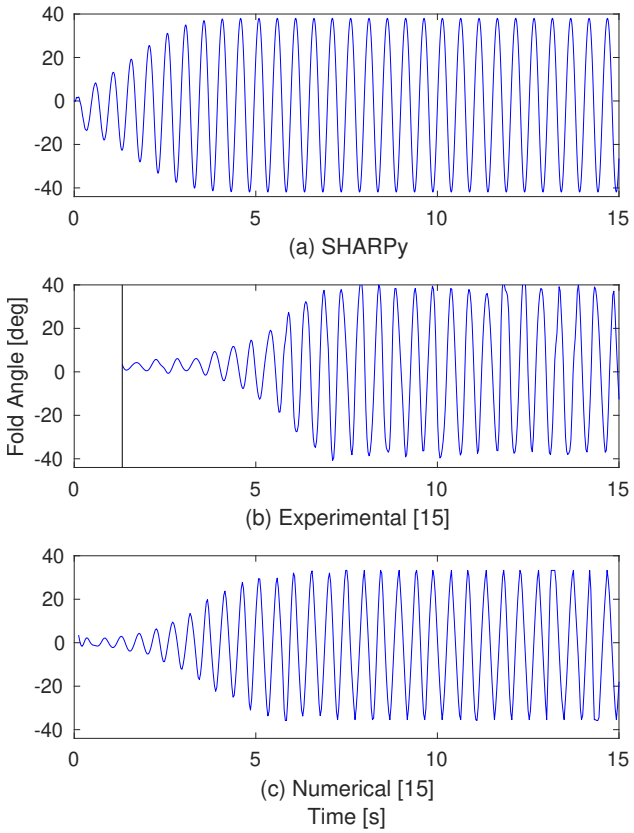


Fig. 5 SHARPy LCO fold angle θ for $u_\infty = 26.8\,\mathrm{m\,s^{-1}}$ and $\alpha = 2.5°$, against numerical and experimental data from [15]

B. Very flexible aircraft

With our verified formulation we now shift our focus to the modelling and analysis of a representative High-Altitude Long-Endurance (HALE) T-tail-configured aircraft, which has been previously used to investigate dynamic aeroelasticity in reduced-order modelling, nonlinear control, wake vortex encounters, maneuvres, amongst others [33, 34]. In the subsequent analyses we have not applied any sectional correction for the lift and drag obtained from the UVLM solution, which in most cases will give us a conservative estimate of loads and displacements and likely system dynamics.

1. HALE and H^2ALE aircraft models

The HALE aircraft, as shown in Figure 6, is configured with a constant-chord, unswept wing of aspect ratio = 32 and a T-tail, powered by a constant thrust force in the material frame forward direction at $\pm 1m$ spanwise from the wing/fuselage intersection, and trimmed for longitudinal flight by means of an elevator deflection input. The flexible wing weighs 24 kg; the rest of the structure weighs 54.25 kg, 50 kg of which is a lumped mass at the wing-fuselage intersection. The numerical model is made parametric with respect to

the dihedral angle of the wing tips, with versions denoted as HALE-dXX where XX is the dihedral angle in degrees. More details on the architecture of the model can be found in [26].

Based on the HALE aircraft model we have built the H^{2}ALE by replacing the dihedral seen at the outboard sections of the wings with a pair of flared hinged wing tips, where they are flush with the inner wing at 0 fold angle. The wing tips are allowed to flap freely and constitute one-fourth of the total span, which should be more than sufficient for the wing-wingtip interactions to be evident [16]. The numerical model is made parametric with respect to the flare angle, with versions denoted as H^{2}ALE-fXX where XX is the flare angle β in degrees. Figure 7 shows the H^{2}ALE aircraft in steady level flight, where as the flare angle increases, the equilibrium fold angle decreases, while bending/twisting of the main wing increases, where Figure 8 shows the H^{2}ALE-f10 in free flight, 2 seconds post gust encounter from trim.

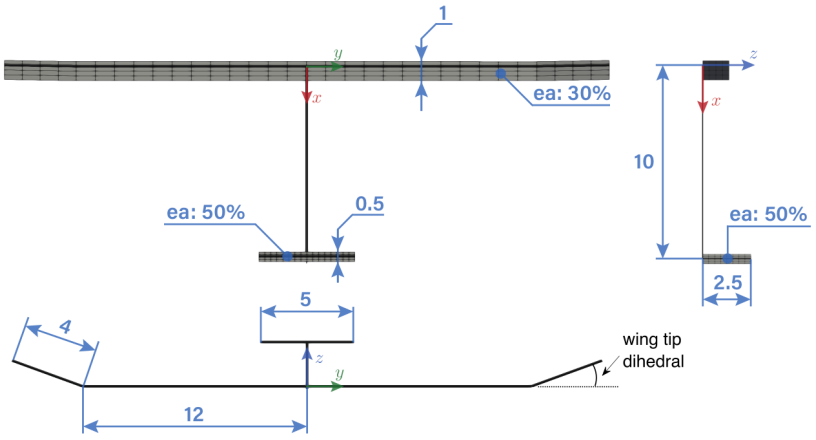


Fig. 6 Geometric definition of the T-tail HALE model with all units in meters as in [26].

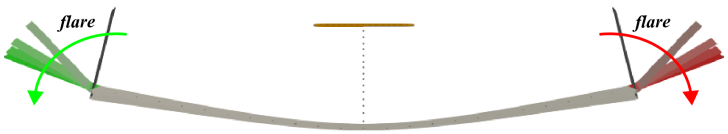


Fig. 7 H^{2}ALE aircraft, with flared hinged wing tips coloured in increasing flare, at trim

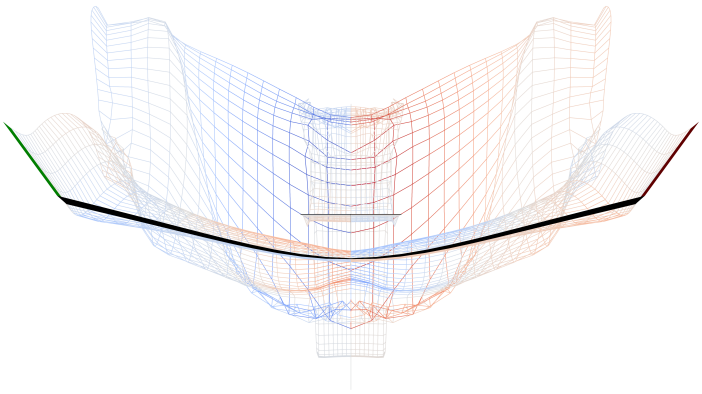


Fig. 8 Snapshot of H^{2}ALE-f10 with force-free UVLM wake grid coloured by circulation intensity, gust length = 15 m, gust intensity = 160% u_∞, 2 seconds post gust encounter

We have first selected the HALE-d00 and the HALE-d90, to compare with the H^{2}ALE-f10 - it is thought that the former configurations would be good proxies of the latter with the flared hinged wing tips locked. A small flare angle of 10 degrees is shown to be enough practically for ensuring the dynamic stability of the hinged wing tips, while having a larger flare angle would extend the stability boundary with respect to sideslip angle [8], but lead to lower damping in the hinge flapping mode. Fundamentally, the H^{2}ALE will have the locked, extended (HALE-d00) and upturned (HALE-d90) configurations as limit cases - its dynamics is shown in subsequent sections to mostly fall in between that of the two references.

2. Aeroelastic trim and equilibrium state

We first trim all three aircraft at a flow velocity of $10\,\mathrm{m\,s^{-1}}$. respectively, using the algorithm described in Section II.A.4. Figure 9 shows the time histories of the control inputs and the relevant states. Note that more steps are required to trim the H^{2}ALE-f10.

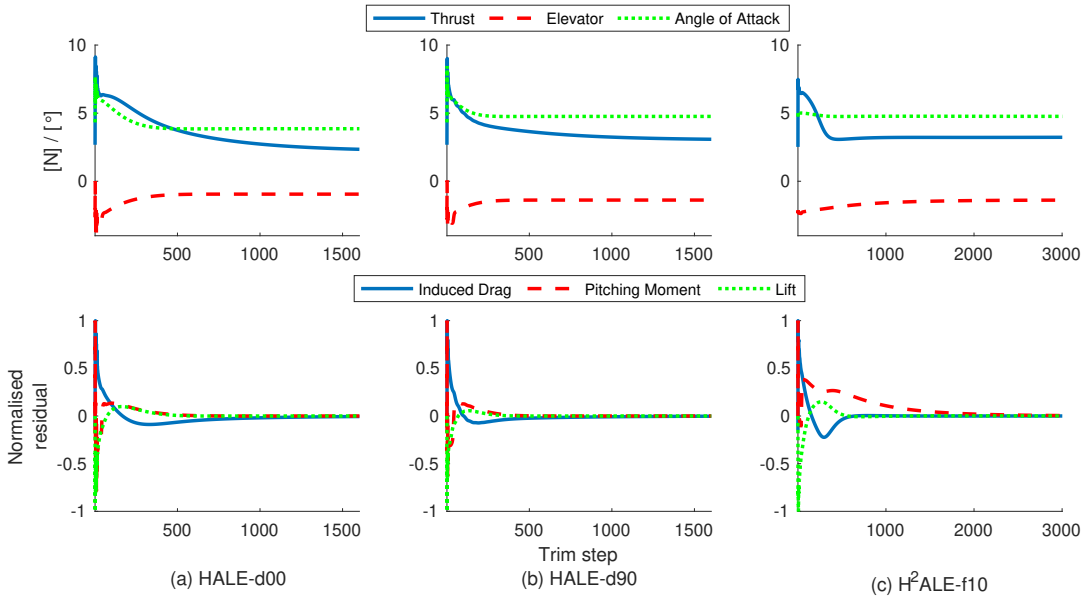


Fig. 9 Trim time histories of control input versus corresponding states

The longitudinal trim values are given in Table 2. We have nondimensionalised the pitching moment and lift by weight multiplied by chord, and weight, respectively. Do note the residual induced drag here, as percentage of thrust, is secondary to the elevator and angle of attack inputs - the thrust only ensures the aircraft is in equilibrium longitudinally. Both the HALE-d90 and H^2ALE-f10 requires a slightly higher angle of attack for longitudinal trim - that is thought to be a result of the partial loss in lift outboard of the hinge, resulting in a higher angle of incidence at the main wing to generate the same overall lift. Elevator and thrust input is likewise higher in magnitude to counteract the extra pitching moment and induced drag due to the higher angle of attack. The tiny residuals in the pitching moment and lift in H^2ALE-f10 are due to the less aggressive action of the PI controllers, and at less than 1%, the impact on the time histories of the aircraft are not evident in the short gust timescales we are subjecting the aircraft to.

Table 2 Comparison of trimmed values for HALE and H^{2}ALE

Values at trim	HALE-d00	HALE-d90	H^{2}ALE-f10
Thrust [N]	2.35	3.08	3.23
Residual Induced Drag [%]	13.1	4.10	0.27
Elevator [deg]	-0.95	-1.38	-1.39
Residual Pitching Moment [%]	0.00	0.00	0.14
Angle of attack [deg]	3.86	4.76	4.76
Residual Lift [%]	0.00	0.00	0.03

3. Vertical gust response

To understand more about the coupled flight dynamics and aeroelastics, we have performed a gust length sensitivity analysis by subjecting each of the three aircraft from their respective trim state defined in Section II.A.4 to 1-cos gusts across an order of magnitude in length centered around the vehicle length (10 m), and constant intensity of 50% u_∞. It is hoped that the gust will then excite the combination of aeroelastics and flight dynamics at different length and time scales, allowing for a comparison of the responses. The tracked variable, wing root bending moment, is chosen because it is thought to be the most critical in a vertical gust encounter. It is nondimensionalised using the product of the aircraft weight and one-eighth span length (4 m). As shown in Figure 10, the H^{2}ALE-f10 has a trim wing root bending moment (WRBM) between the two HALE configurations as predicted, with value much closer to that of HALE-d90 - that implies with the free flared hinge we can almost recover the best case scenario of vertical winglets in terms of alleviating the bending loads at the root.

In terms of the sensitivities, the HALE configurations show a early peak in response, both at the 7.5 m mark, where the H^{2}ALE-f10 peaks at 15 m, suggesting different mechanisms in play especially after the first WRBM peak in response to the gust. We have chosen to compare the gust intensity sweep, from 0 to 160% u_∞, of the three configurations at each of the identified gust lengths. We have intentionally chosen high values for the gust intensity, both to examine the dynamics of the very flexible aircraft configurations at extreme geometric nonlinearities, and to demonstrate robustness of the numerical implementation. Note that no stall model is included.

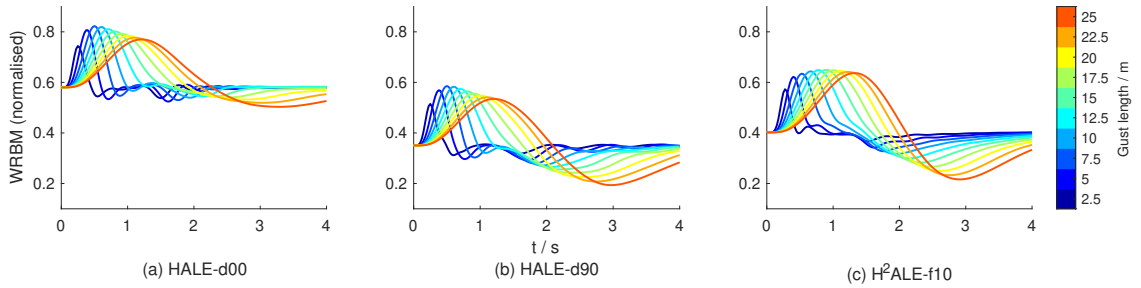


Fig. 10 Time histories of wing root bending moment, normalised by the product of aircraft weight and one-eighth span length, at various gust lengths, gust intensity = 50% u_∞

Gust length = 7.5 m As this is the most sensitive gust length for the HALE configurations, it is perhaps unsurprising that comparing across most gust intensities, both the HALE-d00 and HALE-d90 experience higher maximum transient WRBM than the H^{2}ALE-f10 at the highest gust intensity of 160% u_∞, as evidenced in Figure 11, where in the first row the time histories from trim of the normalised WRBM are shown, and in the second row, the increments in WRBM from the trim case, normalised by the gust intensity, are plotted, with the trends near the first peak included in the inset. Apart from a lower first peak at higher intensities than the HALE-d90, the transient oscillations are more damped than the HALE-d00 with the H^{2}ALE, suggesting the hinge is helpful in this particular setup and conditions to alleviate both the peak and subsequently oscillating gust loads. An example of configuration and conditions where the oscillations are less damped after the peak load is reduced can be seen in [16]. It is worth noting that the WRBM increments as plotted do not exactly coincide as the gust intensity increases - this is because of the geometric nonlinearities captured in the formulation. A close inspection of the first peak would reveal that as we increase the gust intensities, the very presence of the hinges brings about less increment in WRBM per gust intensity unit - suggesting perhaps the additional wingtip flapping motion is extracting more aerodynamic damping to reduce transient loads.

Examining the wing root torsional and bending moment plotted against each other in Figure 12 reveals a few trends - first of all, that the H^{2}ALE-f10 shares similar correlation of bending to torsional loads with the HALE-d00, and that they are much less coupled than in HALE-d90, where the fixed vertical wing tips act as unbalanced masses promoting bending-twisting coupling. In terms of the magnitude of loads experienced, the H^{2}ALE sees loads comparable to the HALE-d90 and significantly smaller than HALE-d00.

In determining the overall load envelope of a particular aircraft configuration Figure 12 demonstrates why it is important to consider the nonlinear dynamics - for the H^{2}ALE-f10, and to a lesser extent the HALE-d90, the largest gust intensity case does not define the entire load envelope.

In addition to the zero moment transfer, a second mechanism of wing root bending moment relief is seen for the H^{2}ALE. At gust onset the inner wing tends to fly up and flex up, and through the hinge by inertia and aerodynamic damping the wing tips tend to fold negatively (seen in Figure 13) - that leads to higher effective angle of attack on the wing tips due to the downwards flapping motion, and higher geometric angle of attack on the wing tips due to flare. All this combined gives upwards (restoring) lift on the wing tips, and hence a downwards (dampening) force is exerted through the hinge on the inner wing, reducing the flex up tendency, itself a self-regulating cycle which in time dampens any transient flexible and hinge motion, as evidenced by Figure 14. Note also the WRBM and z-location of the dihedral / hinge point, respectively in Figures 11 and 14, are almost always in phase, suggesting one is a good proxy for the other, in this largely inertia-driven wingtip assembly.

With this mechanism the momentum of the rigid body motion is converted to the flapping of the wing tips, which is readily dissipated by the aerodynamic forcing - we see marginally higher net vertical position of the hinge, relative to the root (which scales with structural deformation) in exchange for massively reduced rigid body vertical displacement, and improvement in WBRM. This scales well with increasing gust intensity, as aerodynamic damping is predominantly quadratic with respect to increasing velocity.

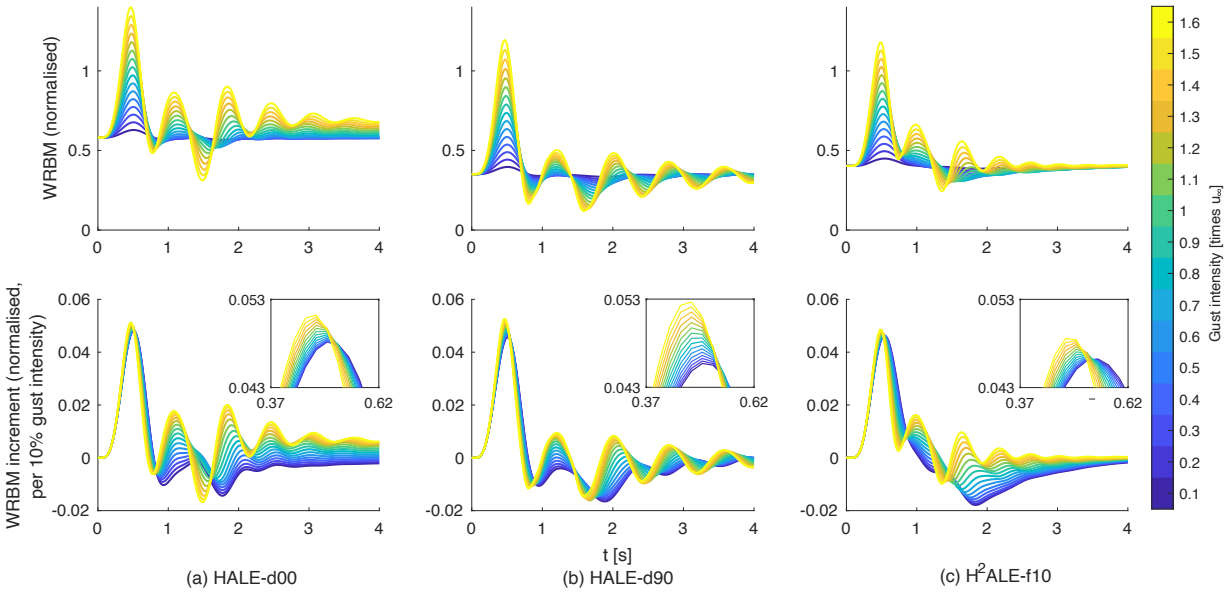


Fig. 11 Time histories of normalised and incremental WRBM over range of gust intensities, gust length = 7.5 m. Moment increment plots include inset with values near the first peak.

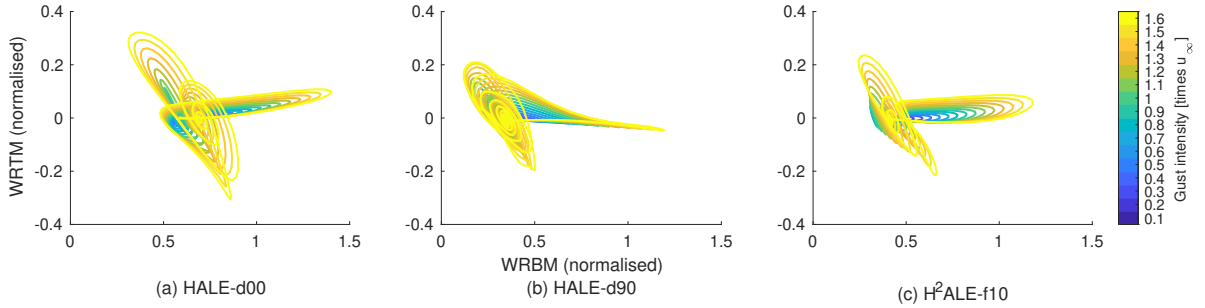


Fig. 12 Instantaneous values of normalised wing root bending and torsional moment over range of gust intensities, gust length = 7.5 m

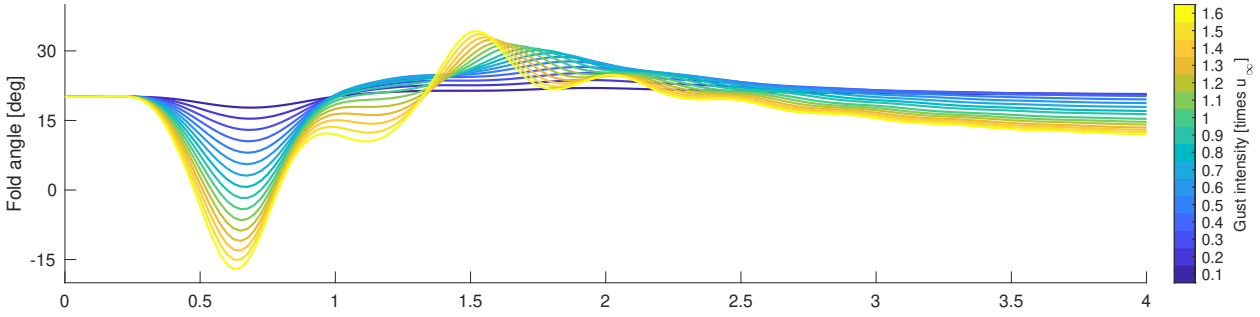


Fig. 13 Time histories of hinge fold angle for the H^{2}ALE-f10, gust length = 7.5 m

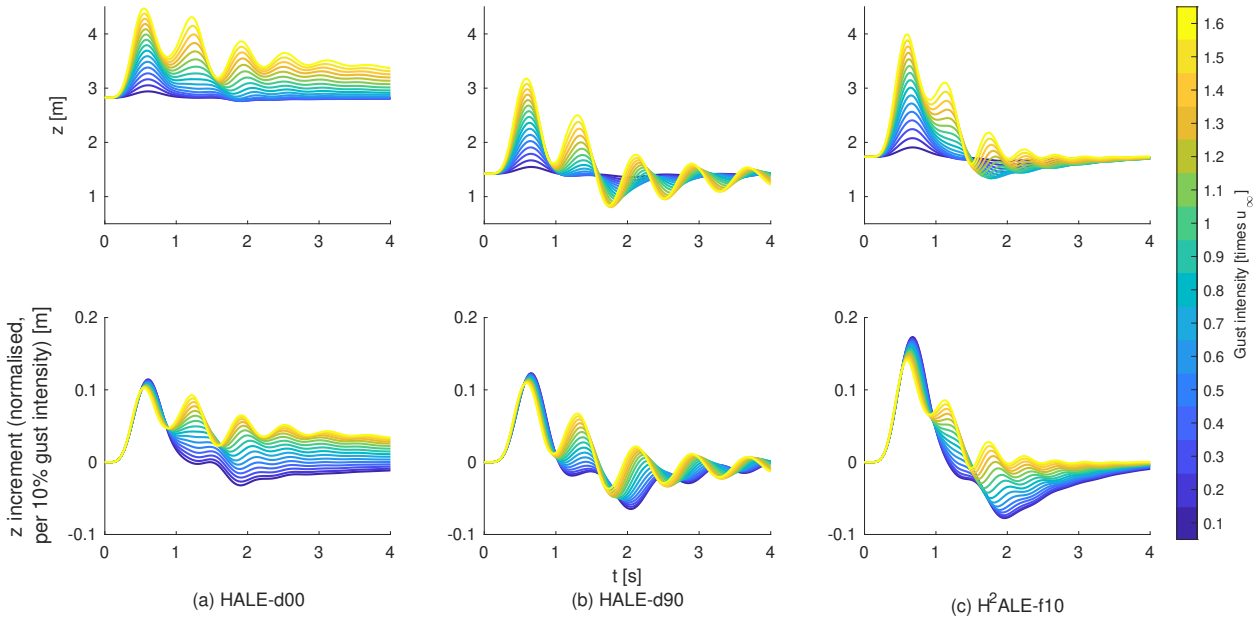


Fig. 14 Time histories of wing dihedral/hinge vertical position relative to root over range of gust intensities, gust length = 7.5 m

Gust length = 15 m This is the most sensitive gust length for the H^{2}ALE-f10 - as evidenced by Figure 15, where the transient WRBM increment due to the longitudinal gust is consistently higher than the HALE

configurations. There is a silver lining to this, since the hinge mechanism results in progressively less WRBM when increasing gust intensity, i.e. nonlinear load relief - something which is not seen in the gust length = 7.5 m case. Torsional and bending moments in Figure 16 shows the same trends.

When we examine the flexible vertical deflection in Figure 18 we recognise the same higher initial peak. Subsequently, and more visibly than with the previous gust length, in terms of the flexible deformation the H^{2}ALE-f10 enjoys the best of both worlds - quicker to settle to equilibrium shape than the HALE-d00, and much more damped oscillations than the HALE-d90, likely due to the dissipative flapping identified earlier. Regarding the fold angle time histories in Figure 17, as the gust intensity increases the higher frequency flapping modes become less damped - becoming a potential source of LCO in the wing assembly.

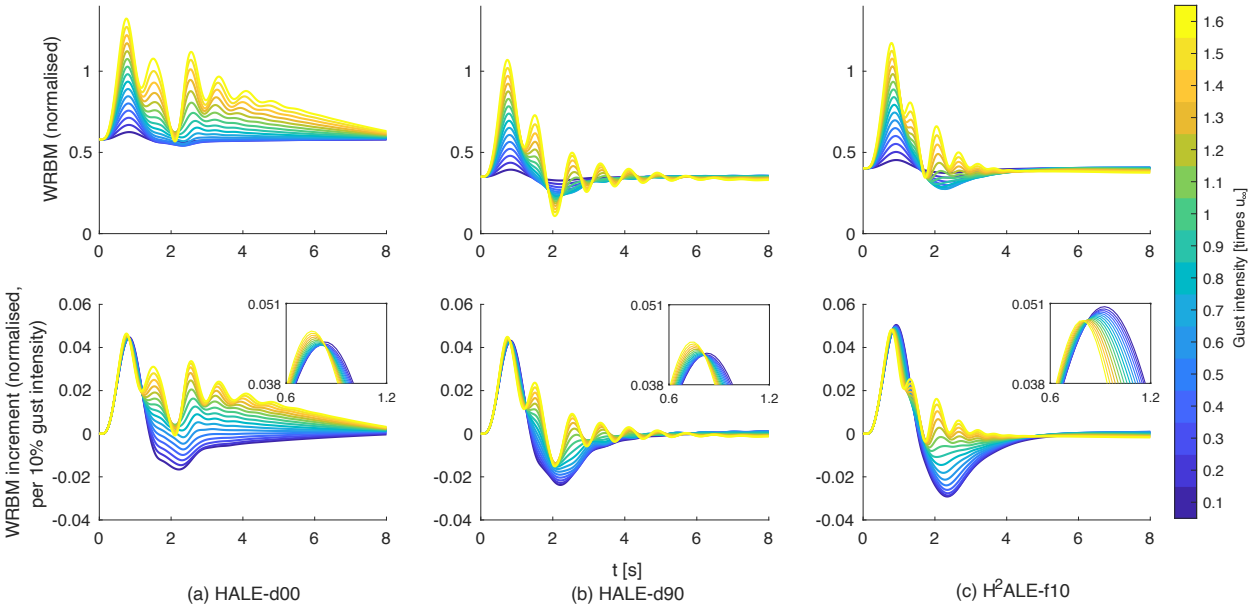


Fig. 15 Time histories of normalised and incremental WRBM over range of gust intensities, gust length = 15 m. Moment increment plots include inset with values near the first peak.

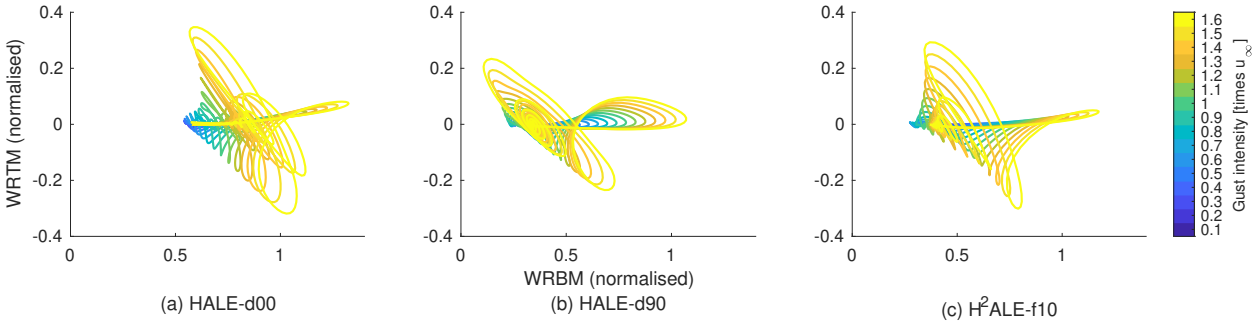


Fig. 16 Instantaneous values of normalised wing root bending and torsional moment over range of gust intensities, gust length = 15 m

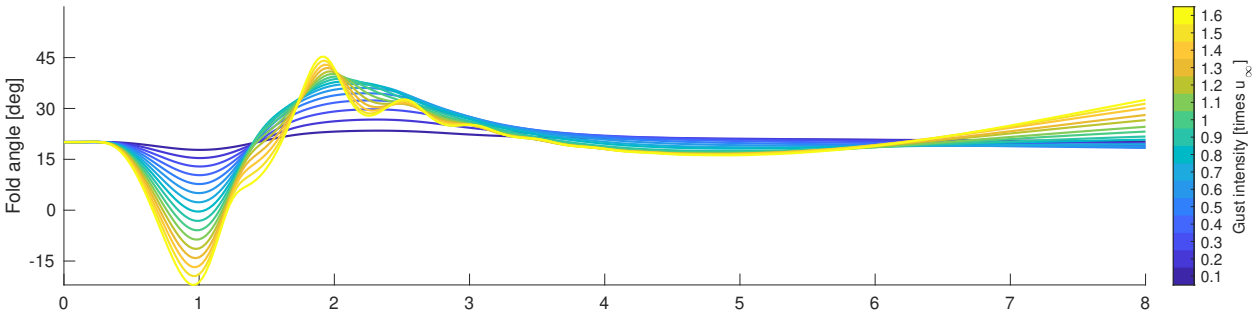


Fig. 17 Time histories of hinge fold angle for the H^{2}ALE-f10, gust length = 15 m

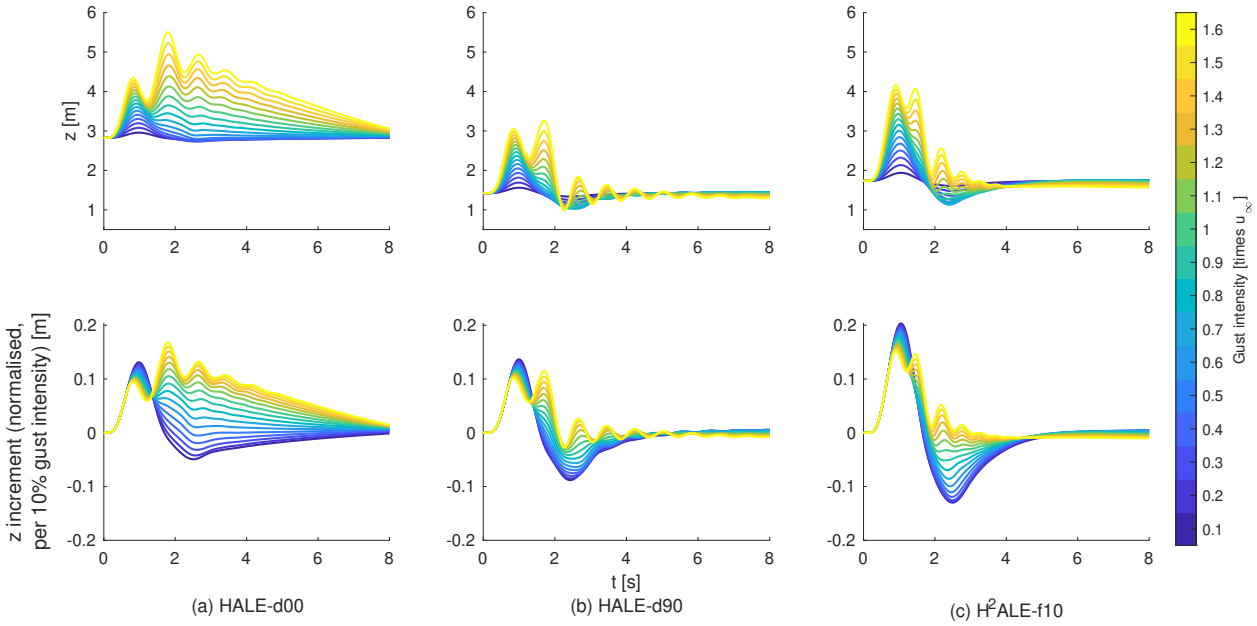


Fig. 18 Time histories of wing dihedral/hinge vertical position relative to root over range of gust intensities, gust length = 15 m

Effect of flare Returning to the physics of the hinges that no moment parallel to the axis are transferred, it is then evident that non-zero flare angles at the hinge would slightly increase trim WRBM, as shown in Figure 19. This penalty is secondary to the presence of the hinge itself. However, maximum penalty occurs at around $\beta = 10°$, then slightly decreases at higher flare angles for the trim WRBM - the effect can be attributed to the steady-state decreasing bending contribution of the lift by the rotated wingtip aerodynamic surface.

For the peak WRBM experienced during the gust encounter, there is a gradual hike from zero flare to again around around $\beta = 10°$, followed by a slight increase towards higher flare angles. The increasing trend is explained by the transient transfer of moment not parallel to the axis - the bending contribution of that

increases with the increasingly slanted hinge axis.

Both of the progressively tapering trends towards higher flare angles can be explained by cross-referencing the fold angle and z flex displacements in Figure 20 in time. They coalesce towards higher flare angles, indicating a similar equilibrium shape leading to a largely similar loading.

It is worth noting that at $\beta = 0$, where the hinge axis is exactly perpendicular to the spanwise direction, we do not experience the theorised loss of stability in the wing tip from a linear analysis [7] - that is due to the bending/twisting coupling of the very flexible wing changing the effective flare angle seen by the flow. It is also remarkable that the amplitude of the hinge motion is largely constant with flare angle, suggesting a weak relationship with the induced geometric angle of attack due to flare in a vertical gust encounter.

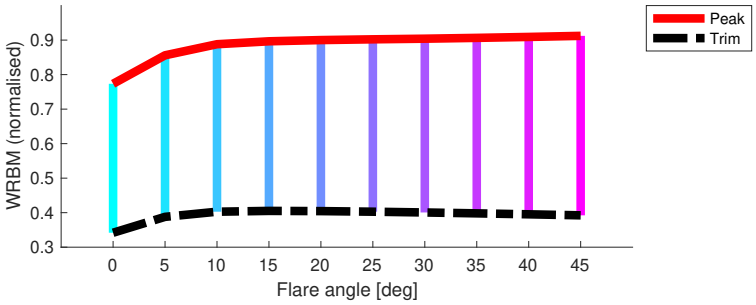


Fig. 19 Range of trim-peak WRBM for H^{2}ALE with varying flare angle, gust length = 15 m, gust intensity = 100% u_∞

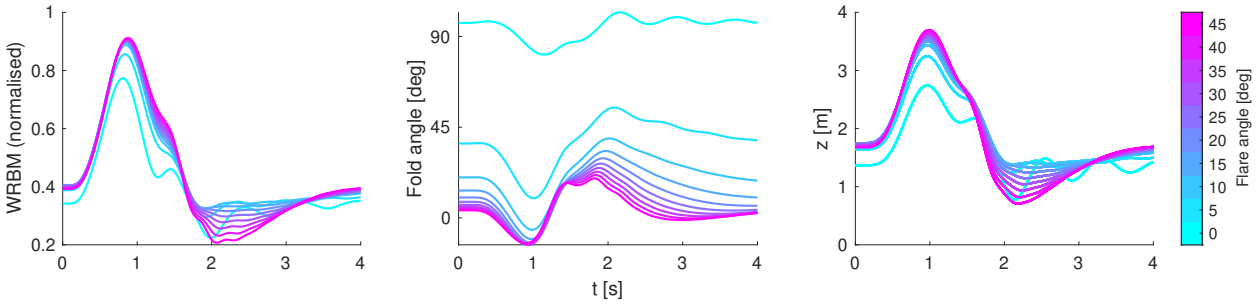


Fig. 20 Time histories of key quantities for H^{2}ALE with varying flare angle, gust length = 15 m, gust intensity = 100% u_∞

Effect of negative flare Since for this particular straight wing configuration we have seen that a zero-flare configuration can still produce stable trim shapes, we turn our attention to negative flare angles, i.e. a hinge axis towards the wing tips downstream, to complete the discussion. Wing tips with the hinge axis pointed in the aforementioned direction is previously thought to be inherently dynamically unstable, at least from a static analysis point of view [7].

Figure 21 shows at $\beta = -35°$ there exists a stable dynamic equilibrium with fold angle close to $-180°$, meaning the wing tips are folded inwards. Conceptually a dynamically stable equilibrium is possible at a negative flare angle with inward-folding wing tips since higher lift on the wing tips mean it folds in even more, where then the flare angle means the geometrical angle of attack is reduced, providing a restoring force. The trim values for WRBM and vertical flexing largely follows the same trend - that they are both larger than the zero flare value. They are however bigger in magnitude than the positive-flare variants, suggesting an inward-folding wing tip configuration is much less efficient.

Examining the gust encounter time history of the fold angle at $\beta = -35°$ reveals a limitation of the model - that the wing tips have actually exceeded the negative 180° physical limit - which in real life would mean the wing tips are in collision with the main wing. This is the only case within this paper where this happens - all other cases shown features dynamics that respects this limit.

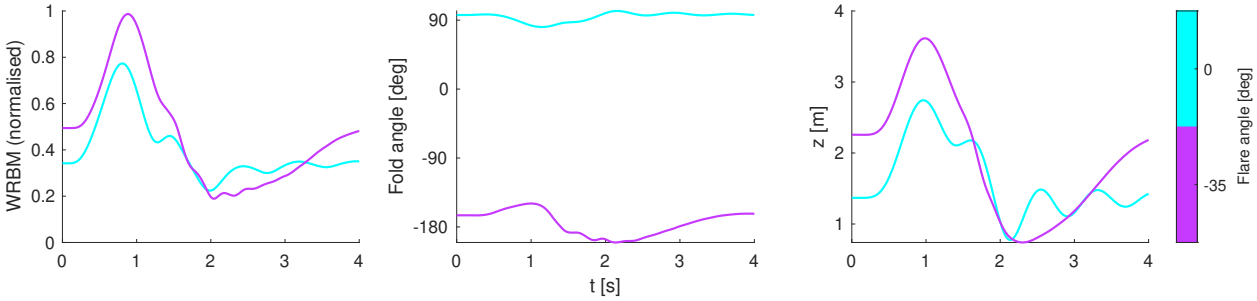


Fig. 21 Time histories of key quantities for H^{2}ALE with $\beta = 0, -35°$, gust length = 15 m, gust intensity = 100% u_∞

Effect of mass distribution The wing tips in the H^{2}ALE configurations are 25% of total span - given also there's no taper in the wing, and it having constant material properties, it can be considered quite a heavy tip, resulting in what is thought to be more inertia-driven dynamics in the past Sections. To address that we have also set up an alternative model with half of the wingtip mass removed and added to the lumped mass at the root, to keep the total wing assembly mass constant.

The gust response in Figure 22 are largely similar in terms of the time histories - except there has been a constant offset at the trim value, and we no longer have a turning point in WRBM vs flare angle as in Figure 20. This explains the secondary WRBM mechanism discussed in Section III.B.3, that increasing flare brings about an additional WRBM penalty, is predominantly an effect due to the mass distribution of the wing and wingtip assembly. In fact, it is perhaps surprising that with less mass at the wing tip more WRBM is seen -

that would be down to the extent bending-torsion coupling is active in the aeroelastic case that changes the spanwise distribution of lift on the wing.

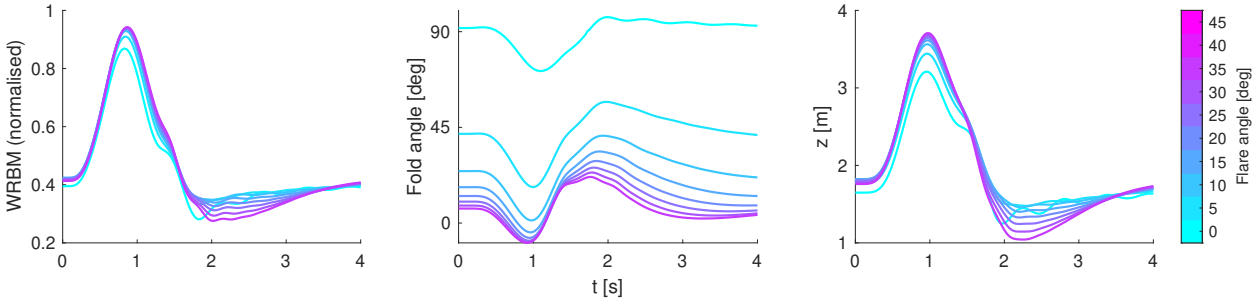


Fig. 22 Time histories of key quantities for H^{2}ALE with varying flare angle (redistributed mass), gust length = 15 m, gust intensity = 100% u_∞

Other results involving also the HALE remain closely aligned with the original mass configuration and hence will be included instead in the accompanying online repository.

Effect of stiffness In an effort to attribute the load alleviation effects seen in Section III.B.3, we have prepared yet another set of alternative HALE and H^{2}ALE models, this time with five times the original stiffness in all directions. With a much stiffer wing assembly we see a clean single cycle response to the 1-cos vertical gust in the WRBM and z-deflection, where subsequent transient fluctuations have high damping. It is also worth noting that the peak values across all configurations are much higher in Figure 23 than in Figure 15 - indicating that the flexible modes do take away energy from the rigid body response, resulting in a substantial load alleviation, which is evident also in Figure 26. It is also evident that in terms of the first peak, as gust intensities increase, the H^{2}ALE-f10 loses its comparative effectiveness in reducing transient WRBM (we also lose the nonlinear load relief identified earlier) - that the hinge itself, and flexibility in the main wing, are both necessary for any load alleviation mechanism identified. The fold angle time histories in Figure 25 compared to Figure 17 indicates the same; that the first negative peak of the fold angle is reduced compared to the flexible model, which is because the main wing flexes much less with the gust encounter and causes less of a inertial downswing of the wing tips.

From Figure 24 we can identify that the H^{2}ALE-f10 sees a larger range of WRBM, where the coupling with the torsional component bears resemblance to both the HALE-d00 and HALE-d90 - more so to the HALE-d00 at lower bending loads (where presumably the dynamics mimic a cantilever wing), and to the HALE-d90 otherwise (where the higher bending loads encourage the wing tip to flap - behaving more like a out of plane mass as in the HALE-d90).

When sweeping through the various variants with different flare angles for H^{2}ALE, the same general trend in higher loads and deflections are identified in Figure 27. The fold angle time history for $\beta = 0$ is perhaps interesting - since the wing tips are pointing almost vertically upwards, and the main wing flexes much less, it is seen that the fold angle range is smaller than the other β cases.

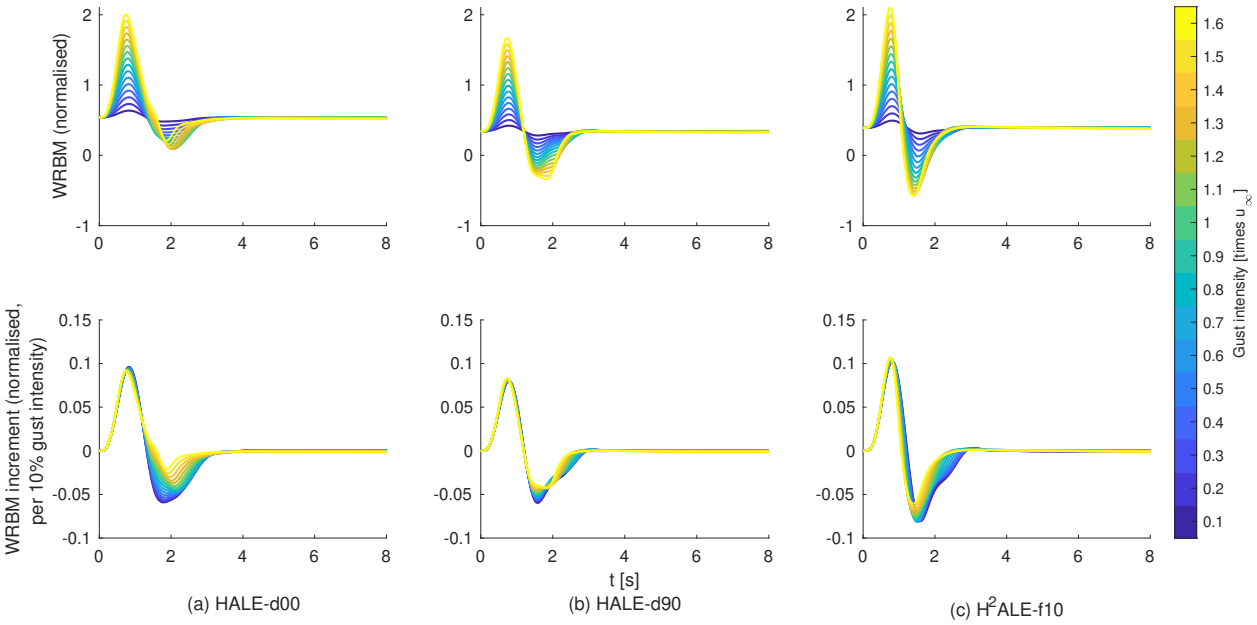


Fig. 23 Time histories of normalised and incremental WRBM over range of gust intensities, gust length = 15 m, stiffened wing assembly

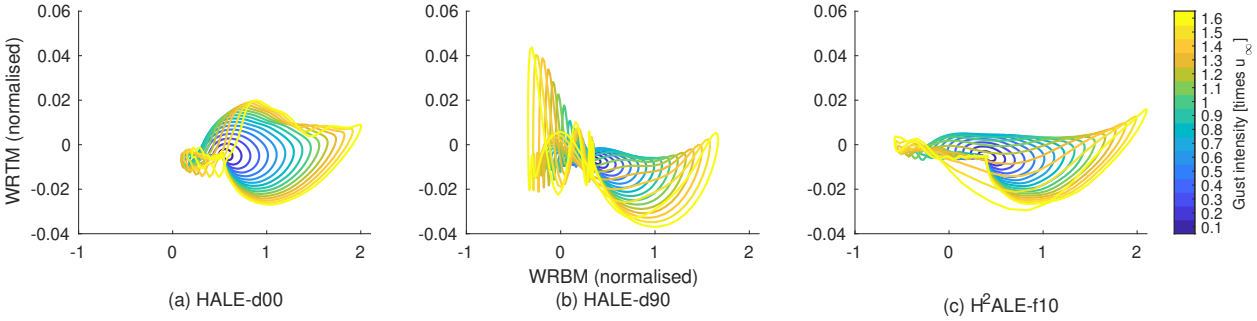


Fig. 24 Instantaneous values of normalised wing root bending and torsional moment over range of gust intensities, gust length = 15 m, stiffened wing assembly

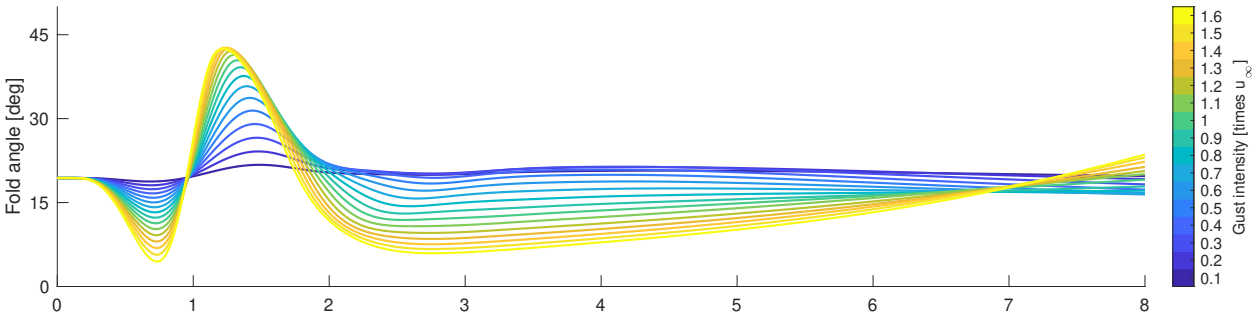


Fig. 25 Time histories of hinge fold angle for the H^{2}ALE-f10, gust length = 15 m, stiffened wing assembly

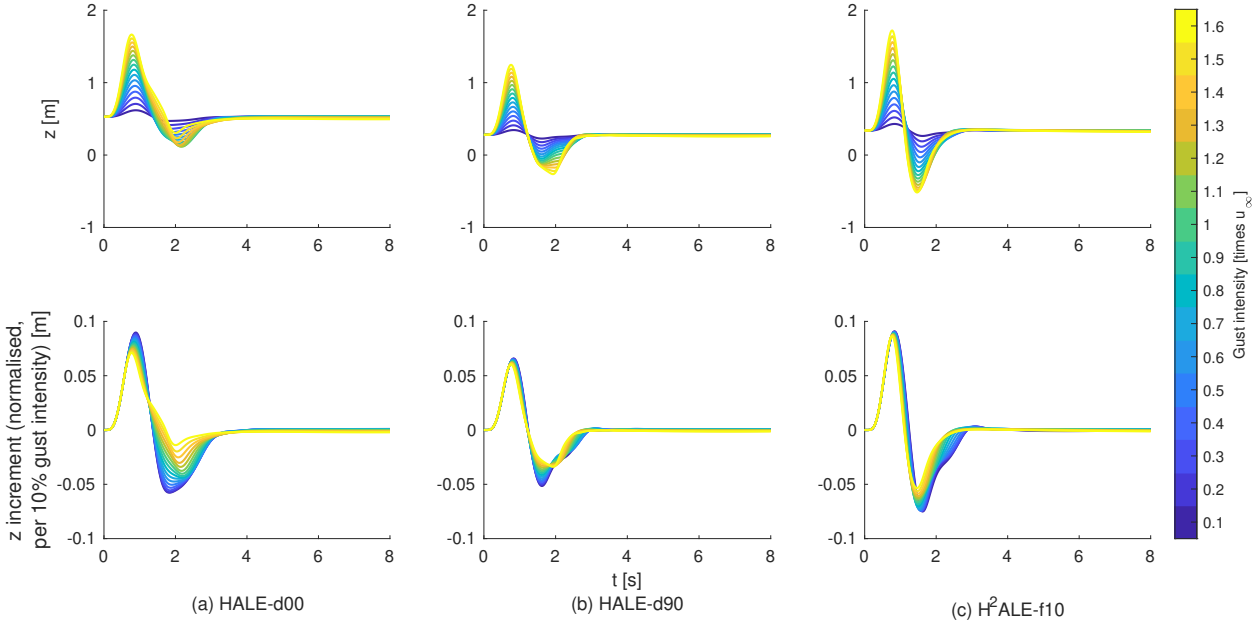


Fig. 26 Time histories of wing dihedral/hinge vertical position relative to root over range of gust intensities, gust length = 15 m, stiffened wing assembly

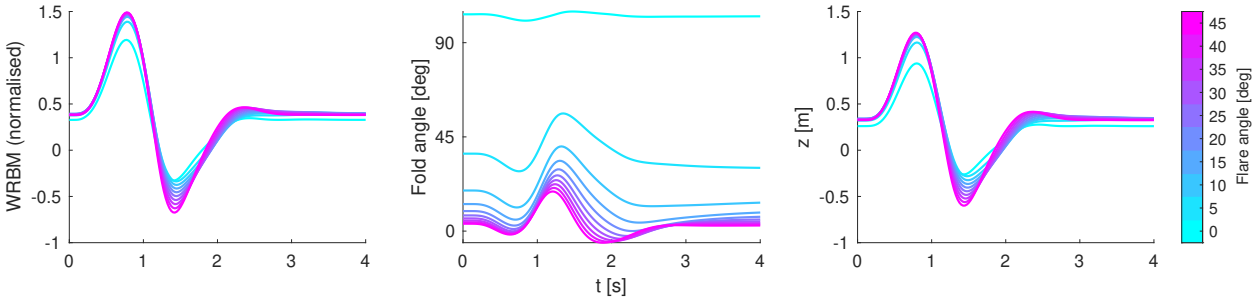


Fig. 27 Time histories of key quantities for H^{2}ALE with varying flare angle (stiffened), gust length = 15 m, gust intensity = 100% u_∞

4. Lateral gust response

The lateral gust response, particularly for the H^{2}ALE, is driven by quite different physics when compared to the vertical gust response. A 1-cos lateral gust to the right (starboard) wing is introduced in all the configurations. For this problem, the wingtip collision at fold angle $= \pm 180°$ is used as the sizing case rather than wing root moments, since the wing moment increments due to a lateral gust are much smaller than the maneuver loads. Hence, in Figure 28 we plot the evolution of the fold angles and roll angle with gust length.

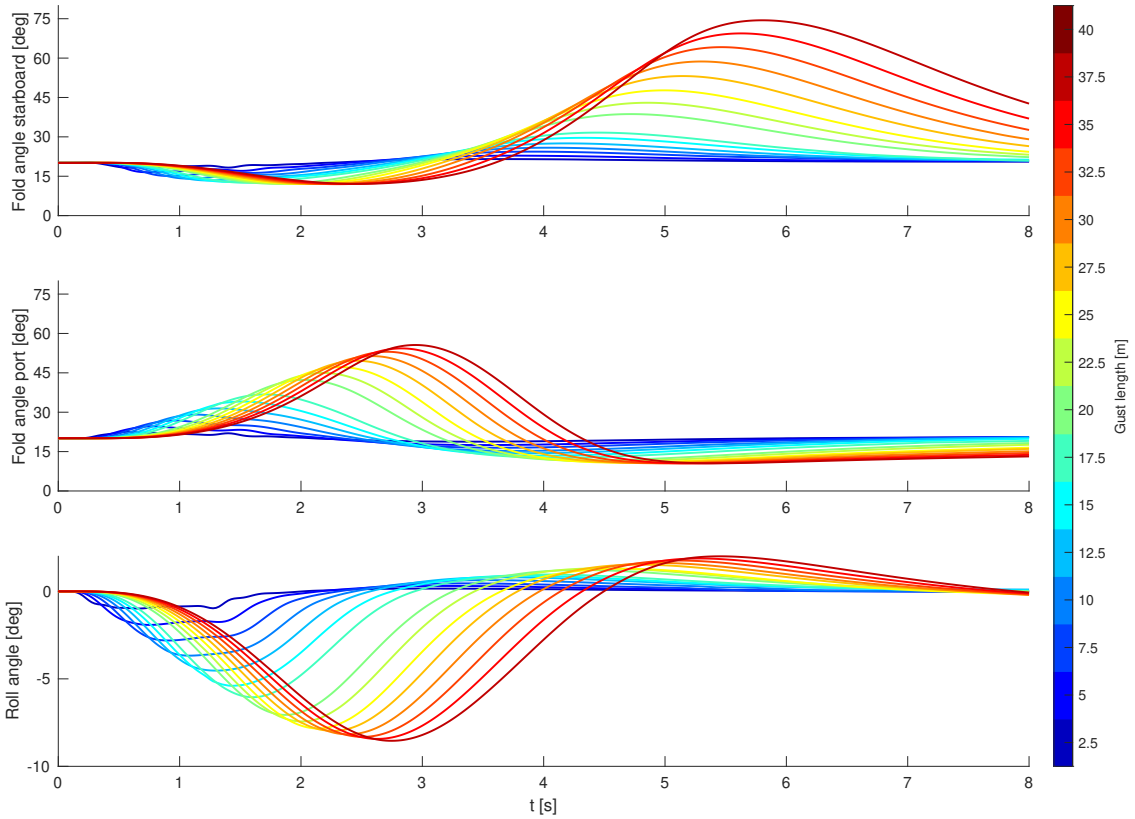


Fig. 28 Time histories of hinge fold angle port and starboard at various lateral gust lengths, gust intensity = 50% u_∞

As it can be seen, roughly for the first 4 seconds after gust onset, the starboard wing tip settled at a smaller fold angle than trim which does not scale with gust length, while the port wing tip promptly increases largely linearly with gust length. The opposite occurs in the subsequent 4 seconds, after which the fold angle on both wing tips approaches the trim value. From the roll angle subplot we recognise for the first 4 seconds after gust onset the aircraft rolls to the right and back, and for the subsequent 4 seconds the roll angle remains almost zero. We have chosen gust length equal to 15 m as before for a reasonable range of fold angle, as well as a good mix of wing tip and rigid body driven flight dynamics. For subsequent analyses the intensity sweep is limited to a maximum of 60% u_∞ to prevent unwanted wake defects causing numerical

issues in the time marching simulations.

We have plotted all the Euler angles (roll Φ, pitch Θ, and yaw Ψ) and their time derivatives in Figure 29 - as the aircraft is in steady level flight before the gust hits all parameters other than Θ begin at 0, and that Θ at trim is dependent on the aircraft configuration. Comparing the roll angle response we find the HALE-d90 has the highest roll stability out of the three, whereas the HALE-d00 reached the highest roll angle. The roll rates follow a different evolution: for the first peak the H^2ALE-f10 showed the lowest angular roll velocity across gust intensity levels amongst the three configurations, indicating a higher roll damping, similar to the vertical gust scenario where there are lower increments in WRBM with increasing gust intensity. These can both be attributed to the flapping motion allowing for dissipation. The pitch angle and the time derivative show a similar trend where H^2ALE-f10 has smaller magnitudes than the HALE-d00. The HALE-d90 demonstrates fundamentally different physics - as the aircraft rolls there is a tendency to pitch down rather than up, and it yaws in the different direction (right wing aft) as the plane banks right, which indicates the worsening spiral mode characteristics with the fixed-upwards wing tips. Time histories of the yaw angle and its derivative remains constant across HALE-d00 and H^2ALE-f10, suggesting in the flight dynamics timescale the free wing tips has a negligible impact at least in the directional flight characteristics. From the time histories of the port and starboard fold angles in Figure 31, it is perhaps interesting to see the fold angle histories are approximately in the same timescale as the roll angle history. Hence the wing tips in H^2ALE-f10 are the first to react to the gust, and is subsequently driven by the inertial of the wing tips and flight dynamics. At the gust encounter, the positive-y forcing on the each of the wing tips pushes the starboard tip down and port tip up, and because the hinge moment imparted by the aerodynamic force increase with fold angle up to $\pm 90^\circ$ due to geometry, port fold angle magnitudes are higher. They then reverse direction as the restoring motion from the flight dynamic modes dominate. The two phases are identified and differentiated also by looking at the hinge vertical position history in Figure 30; during the first 3 seconds when the port fold angle increases, the aircraft is rolling to the starboard side and back due to the gust excitation, and the subsequent restoring wing tip dynamics with higher starboard fold angle at almost no roll.

The same effect is then seen with a sweep in flare, as shown in Figure 32 at zero flare, fold angles are amplified due to the larger moment arm. Only a reasonably small ($<15^\circ$) flare angle is needed to keep the working range of the fold angle small, much like the vertical gust analysis. With a flexible aircraft configuration, there exists a trade-off between higher fold angles in lateral gust, and higher WRBM in vertical gust, when selecting an appropriate flare angle.

5. Discussion

It must be noted before we further discuss the observations on the multiple HALE vs H^{2}ALE configurations that these aircraft are by nature highly flexible and nonlinear, and are designed for very different objectives than most of the current candidate models for commercial transport aircraft featuring flared hinged wing tips. However, the observations made will underscore the ability of the formulation to model and predict the coupled dynamics involved, giving confidence to future applications on heavier and stiffer configurations.

In terms of the static wing root bending load alleviation in vertical gust, this is shown to be primarily a feature of the hinge mechanism - and is a weak function of all other variables. Notably, the WRBM of all H^{2}ALE subconfigurations closely approach the HALE-90, i.e. the fixed upturned wing tip case, demonstrating exceptional efficiency. Across increasing flare angle, there is a turning point of maximum WRBM at around $\beta = 15°$, implying opposing mechanisms of load alleviation at different flare angle regimes. A negative flare angle, while is shown to be stable at $\beta = -35°$, drastically increases static WRBM and hence is not desirable for this particular configuration. Lower ratio of wing tip versus root mass actually encourages the coalescence of WRBM at the higher value across flare angles. It is thought that in this case the weight of the wingtip mass helped attenuate lift-induced bending.

As in the dynamic load alleviation in vertical gust, the HALE is most sensitive to the shorter gust length 7.5 m, while the H^{2}ALE the longer 15 m. At higher gust lengths the incremental H^{2}ALE response can be the most severe out of the three compared configurations, but the 1g+gust response remains bounded by the HALE-d00 and the HALE-d90, a trend which is seen across different variables investigated. A comparison of the first positive (wing tip up) peak increment loads normalised by gust intensity shows cases where the increment on H^{2}ALE is slightly larger than the HALE cases, but at both gust lengths there are nonlinear effects at higher gust intensities that the H^{2}ALE only can leverage to reduce the increments. In terms of flare angle, peak WRBM get slightly higher for increasingly positive flare angles, and much like the static load alleviation, much higher for negative flare. For a stiffened wing assembly, dynamic loads get worse - the loss of flexibility i.e. elastic potential energy as a sink for the energies in excited rigid-body modes affects the H^{2}ALE-f10 more so than the two HALE comparisons, since the incremental gust loads outpaces the savings in the static 1g load. The first negative peak is masked by flexibility likewise, but especially in the H^{2}ALE-f10 - in the stiffened case the main wing of the H^{2}ALE-f10 gradually transitions into bending downwards transiently with increasing gust intensity.

The performance of H^{2}ALE in lateral gusts is constrained by the maximum fold angle, as one seeks to avoid the wing tips flipping and striking the main wing. Across gust intensities in a lateral gust encounter the H^{2}ALE-f10 shows maximum instantaneous roll angle attained as proxy for roll stability in between the two HALE configurations, and maximum time derivative of roll angle as proxy for roll damping the highest amongst the three configurations. The roll dynamics are mostly coupled with pitching, where yaw seen in H^{2}ALE-f10 seems unaffected at all by the addition of the hinge and is virtually identical to that of HALE-d00, whilst a fundamentally difference response is seen in the HALE-d90.

The H^{2}ALE have demonstrated qualitatively higher damping across all the flare angles investigated. They also tend to return to the equilibrium value fastest, where generally in the HALE-d00 the steady-state error takes time to dissipate, and in the HALA-d90 oscillations are under-damped. Rolling characteristics in lateral gust showed mixed results, with slightly impeded roll performance in exchange for a similar gain in stability. At higher gust intensities, from the inspection of fold angle histories, there is the risk of exciting the higher frequency modes which might escalate into an LCO.

Overall speaking, it is shown that statically the inertia of the wing tip determines the maximum possible WRBM savings in vertical gust, which is leveraged by a careful choice of flare angle with the hinged wing tips. Dynamically the actual WRBM savings achieved is a strong function of wing flexibility, and weaker functions of flare angle, gust length and intensity. These act as sources of nonlinear effects in the vertical and lateral gust responses alike that complicate the coupled aeroelastics and flight dynamics.

We have not included a stall model on the aerofoil polars, a major source of aerodynamic nonlinearity. This is due to its role, in the gust problem considered thus far, of providing extra attenuation of loads. Finally, considerable effort was dedicated to determining the trim state of the system, by exploring suitable gain values for the PI controllers for angle of attack, elevator deflection, and thrust, as functions of the geometrical and inertial properties of the aircraft. The challenge is for them to enable sufficient control authority, while not inducing unsteady system dynamics particularly by large displacements in the UVLM grid. The derivative control did little to influence the performance of the trim routine and hence has been left out.

The difficulty of solving a stiff numerical system comprising dynamics across scales in flight dynamics, aeroelasticity, and multibody dynamics is overcome with the careful choice of the time-integration scheme, extra numerical structural damping, appropriate scaling of the equations, and relaxation across the fluid-

structural solutions. In cases where the Lagrange multipliers do not converge readily, in particular when the hinge is experiencing high transient excitation loads, it is discovered that errors propagate to the geometrical definition (location and rotation) of the hinge nodes, and subsequently skews the instantaneous hinge axis, giving rise to incorrect aerodynamic forcing, eventually leading to numerical divergence. This issue is largely mitigated by posing an additional constraint that the hinge nodes each take the averaged location in the Earth frame, and hence are exactly coincident at every time step. That minimises the constraint force to achieve the hinge constraint and hence encourages convergence of the Lagrange multipliers.

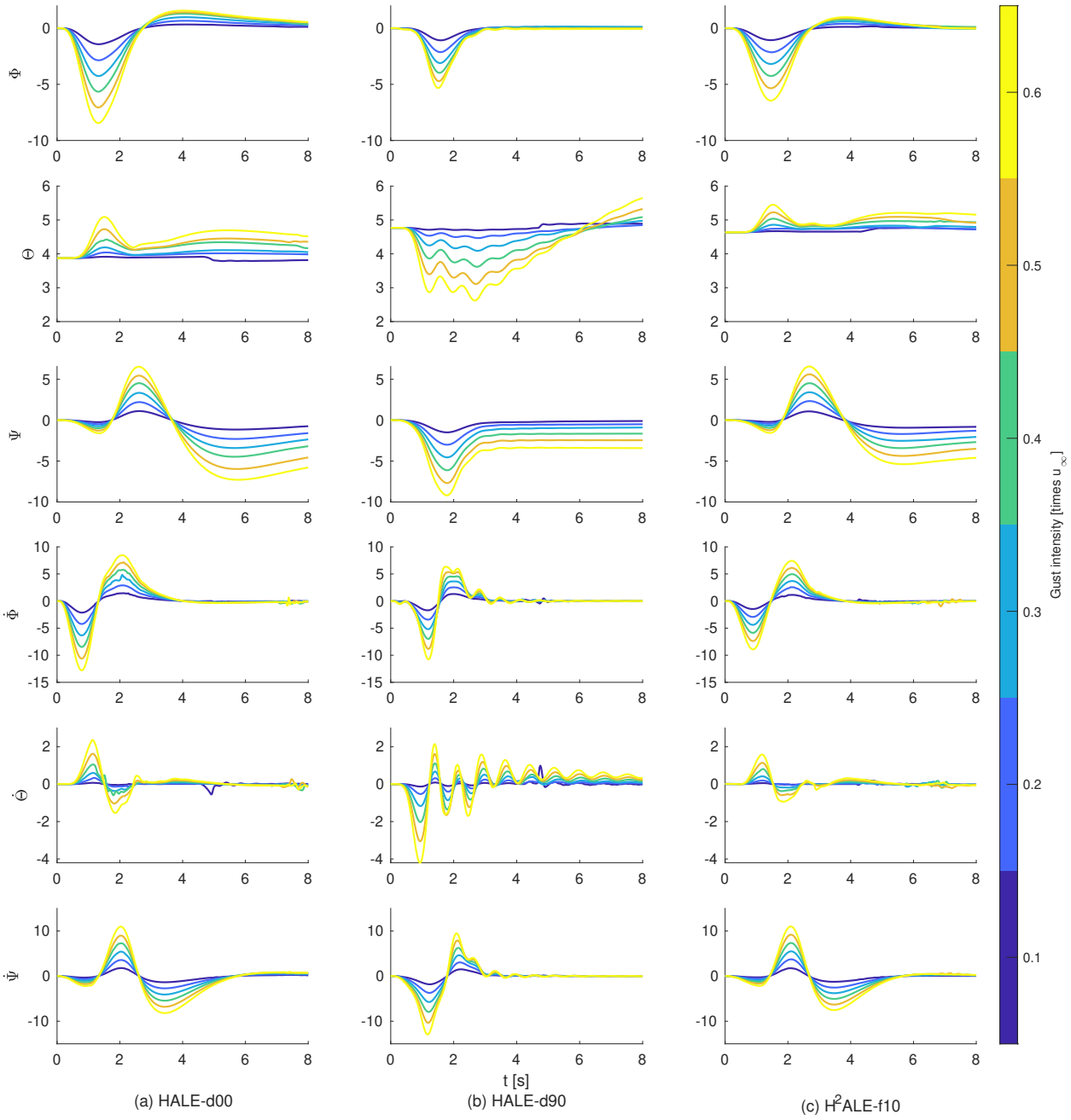


Fig. 29 Time histories of Euler angles in degrees and their derivatives (deg / s) at the wing root, over a range of gust intensities for lateral gust length of 15 m

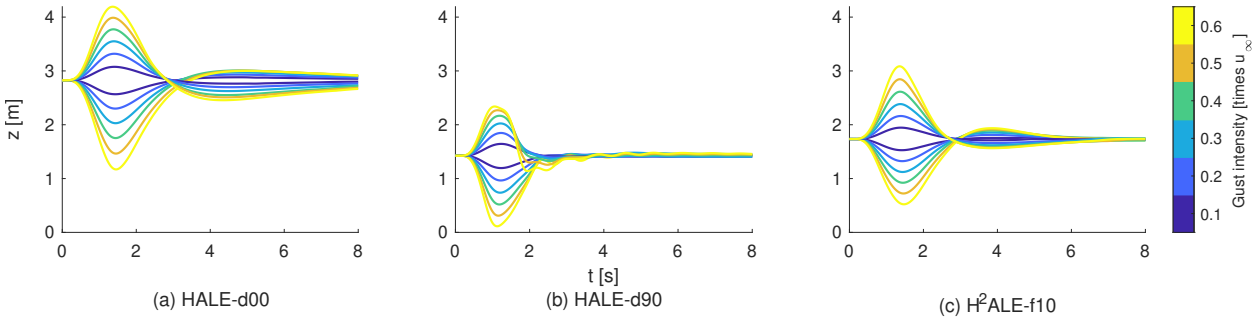


Fig. 30 Time histories of wing dihedral/hinge vertical positions port and starboard, relative to root, over range of gust intensities, lateral gust length = 15 m

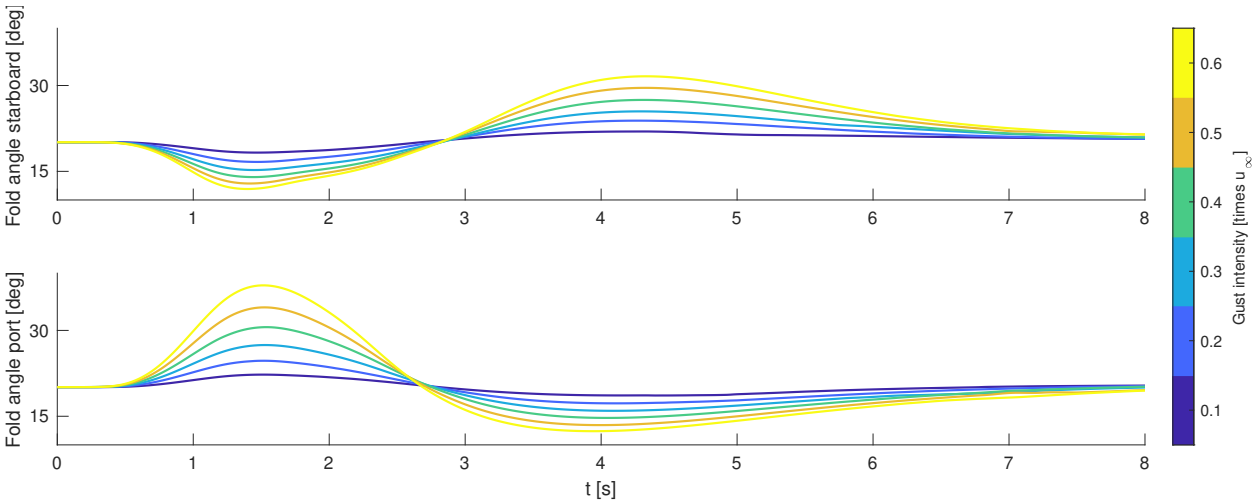


Fig. 31 Time histories of hinge fold angle for H^{2}ALE-f10 port and starboard, relative to root, over range of gust intensities, lateral gust length = 15 m

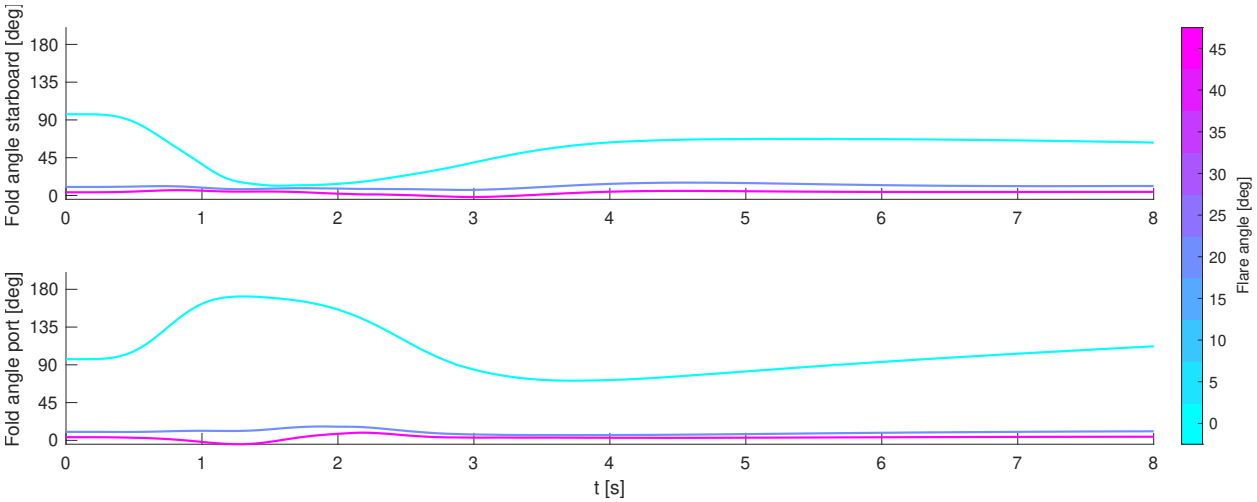


Fig. 32 Time histories of hinge fold angle port and starboard, for various flare angle, gust length = 15 m, lateral gust intensity = 100% u_∞

IV. Conclusions

In this work we have presented a flexible multibody methodology of model aircraft with the flared hinged wings, and verified it against geometrically-nonlinear MSC NASTRAN simulations. A first principles model implemented in MATLAB has also provided a reference for the numerical results on a rigid configuration. The implementation has demonstrated great robustness even with relatively coarse discretisation. A aeroelastic test case involving a flexible wing and wingtip assembly based on literature was set up, with results showing good agreement with published data. The current approach compares well with the experimental results even when geometrically nonlinear effects become more important.

This nonlinear aeroelastic multibody formulation enables coupled flight dynamics and aeroelasticity analysis on aircraft featuring flared hinged wings. An accelerated method for trim has been developed. We can, in particular over existing frameworks, perform unsteady time-domain analyses, incorporating both geometrical and aerodynamic nonlinearities, of free-flying very-flexible multibody aircraft, with different initial and loading conditions. Stall corrections can be added to the aerodynamic description of the model, and has been included in Section III.A. As a demonstration of the capabilities, we focus on the simulation of a High-Altitude Long-Endurance (HALE) T-tail aircraft. A representative model featuring flared hinged wing tips, H^{2}ALE, has been proposed, which is based on a previous HALE aircraft model. A method for trim has been developed and applied to obtain equilibrium states, which are computed for both models with converged respective control inputs. A vertical gust sweep in length and intensity, and subsequently a lateral gust sweep in intensity, has been performed on a range of HALE and H^{2}ALE subconfigurations to better understand the coupled aeroelastics and flight dynamics in play. In extending this work to the analysis of a representative next-generation aircraft model, the effect of wing sweep is expected to alter the trends uncovered in the HALE and H^{2}ALE models.

Problems of interest that can now be investigated include transient loading during maneuvers and gust encounters, the effect of release timing of the wing tips, passive and active load alleviation with the wing tips, performance evaluation, benchmarking, and establishing the nonlinear limit cases of aircraft with such wing assemblies. Those will be topics of future research.

Acknowledgements

We would like to gratefully acknowledge the invaluable data and advice from Fintan Healy in determining the structural properties of the model described in [12, 15], which led to the set-up of the SHARPy model for

the comparison in Section III.A. The work has been supported in part by an Industrial Cooperative Award in Science and Technology [EP/W522004/1] between the UK Engineering and Physical Sciences Research Council and Airbus UK.

References

[1] ATI, "Destination Zero - The Technology Journey to 2050," *ATI Technology Strategy 2022 - Destination Zero*, 2022.

[2] Wunderlich, T. F., Dähne, S., Reimer, L., and Schuster, A., "Global aerostructural design optimization of more flexible wings for commercial aircraft," *Journal of Aircraft*, Vol. 58, No. 6, 2021. https://doi.org/10.2514/1.C036301.

[3] Miceli, M. F., Ameduri, S., Dimino, I., Pecora, R., and Concilio, A., "A Preliminary Technology Readiness Assessment of Morphing Technology Applied to Case Studies," *Biomimetics*, Vol. 8, No. 1, 2023. https://doi.org/10.3390/biomimetics8010024.

[4] Ameduri, S., and Concilio, A., "Morphing wings review: aims, challenges, and current open issues of a technology," *Proceedings of the Institution of Mechanical Engineers, Part C: Journal of Mechanical Engineering Science*, Vol. 237, No. 18, 2023. https://doi.org/10.1177/0954406220944423.

[5] Castrichini, A., Wilson, T., Saltari, F., Mastroddi, F., Viceconti, N., and Cooper, J. E., "Aeroelastics Flight Dynamics Coupling Effects of the Semi-Aeroelastic Hinge Device," *Journal of Aircraft*, Vol. 57, No. 2, 2020, pp. 333–341. https://doi.org/10.2514/1.C035602.

[6] Wilson, T., Castrichini, A., Azabal, A., Cooper, J., Ajaj, R., and Herring, M., "Aeroelastic Behaviour of Hinged Wing Tips," *International Forum on Aeroelasticity and Structural Dynamics, IFASD 2017*, Como, Italy, 2017.

[7] Castrichini, A., Siddaramaiah, V. H., Calderon, D., Cooper, J., Wilson, T., and Lemmens, Y., "Preliminary investigation of use of flexible folding wing tips for static and dynamic load alleviation," *The Aeronautical Journal*, Vol. 121, No. 1235, 2017, pp. 73–94. https://doi.org/10.1017/aer.2016.108.

[8] Conti, C., Saltari, F., Mastroddi, F., Wilson, T., and Castrichini, A., "Quasi-Steady Aeroelastic Analysis of the Semi-Aeroelastic Hinge Including Geometric Nonlinearities," *Journal of Aircraft*, Vol. 58, No. 5, 2021, pp. 1168–1178. https://doi.org/10.2514/1.C036115.

[9] Mastracci, P., Saltari, F., Mastroddi, F., Wilson, T., and Castrichini, A., "Unsteady Aeroelastic Analysis of the Semi Aeroelastic Hinge Including Local Geometric Nonlinearities," *AIAA Journal*, Vol. 60, No. 5, 2022, pp. 3147–3165. https://doi.org/10.2514/1.J061108.

[10] Balatti, D., Khodaparast, H. H., Friswell, M. I., Manolesos, M., and Castrichini, A., "Experimental and numerical investigation of an aircraft wing with hinged wingtip for gust load alleviation," *Journal of Fluids and Structures*, Vol. 119, 2023, p. 103892. https://doi.org/10.1016/j.jfluidstructs.2023.103892.

[11] Cheung, R. C. M., Rezgui, D., Cooper, J. E., and Wilson, T., "Testing of Folding Wingtip for Gust Load Alleviation of Flexible High-Aspect-Ratio Wing," *Journal of Aircraft*, Vol. 57, No. 5, 2020, pp. 876–888. https://doi.org/10.2514/1.C035732.

[12] Healy, F., Cheung, R., Rezgui, D., Cooper, J., Wilson, T., and Castrichini, A., "On the Effect of Geometric Nonlinearity on the Dynamics of Flared Folding Wingtips," *Journal of Aircraft*, Vol. 60, No. 2, 2023, pp. 368–381. https://doi.org/10.2514/1.C036877.

[13] Healy, F., Rezgui, D., and Cooper, J. E., "Experimental Effect of Sideslip Angle on the Dynamic Behaviour of Flared Folding Wingtips," *AIAA SCITECH 2023 Forum*, American Institute of Aeronautics and Astronautics, Reston, Virginia, 2023. https://doi.org/10.2514/6.2023-0376.

[14] Carrillo Córcoles, X., Mertens, C., Sciacchitano, A., van Oudheusden, B. W., De Breuker, R., and Sodja, J., "Effect of Wing Stiffness and Folding Wingtip Release Threshold on Gust Loads," *Journal of Aircraft*, 2023, pp. 1–20. https://doi.org/10.2514/1.C037108.

[15] Healy, F., Cheung, R., Rezgui, D., Cooper, J., Wilson, T., and Castrichini, A., "Experimental and Numerical Nonlinear Stability Analysis of Wings Incorporating Flared Folding Wingtips," *Journal of Aircraft*, 2023, pp. 1–15. https://doi.org/10.2514/1.C037167.

[16] Cooper, J. E., Gu, H., Ricci, S., Toffol, F., Adden, S., Meheut, M., Benard, E., and Barabinot, P., "CS2-THT U-HARWARD Project: Final Assessment and Project Outcomes Evaluation," *AIAA SCITECH 2024 Forum*, American Institute of Aeronautics and Astronautics, Reston, Virginia, 2024. https://doi.org/10.2514/6.2024-2111.

[17] Gu, H., Healy, F., Constantin, L., Rezgui, D., Lowenberg, M., Cooper, J. E., Wilson, T., and Castrichini, A., "Aeroelastic Scaling of a High-Aspect-Ratio Wing Incorporating a Semi-Aeroelastic Hinge," *AIAA Journal*, 2024, pp. 1–13. https://doi.org/10.2514/1.J063646.

[18] Healy, F., Cheung, R., Neofet, T., Lowenberg, M., Rezgui, D., Cooper, J., Castrichini, A., and Wilson, T., "Folding Wingtips for Improved Roll Performance," *Journal of Aircraft*, Vol. 59, No. 1, 2022, pp. 15–28. https://doi.org/10.2514/1.C036372.

[19] Sanghi, D., Cesnik, C. E. S., and Riso, C., "Roll Maneuverability of Transonic High-Aspect-Ratio-Wing Aircraft with Flared Folding Wingtips," *Journal of Aircraft*, 2024, pp. 1–14. https://doi.org/10.2514/1.C037470.

[20] del Carre, A., Muñoz-Simón, A., Goizueta, N., and Palacios, R., "SHARPy: A dynamic aeroelastic simulation toolbox for very flexible aircraft and wind turbines," *Journal of Open Source Software*, Vol. 4, No. 44, 2019, p. 1885. https://doi.org/10.21105/joss.01885.

[21] Lunk, C., and Simeon, B., "Solving constrained mechanical systems by the family of Newmark and α-methods," *ZAMM - Journal of Applied Mathematics and Mechanics / Zeitschrift für Angewandte Mathematik und Mechanik*, Vol. 86, No. 10, 2006, pp. 772–784. https://doi.org/10.1002/zamm.200610285.

[22] Arnold, M., and Brüls, O., "Convergence of the generalized-α scheme for constrained mechanical systems," *Multibody System Dynamics*, Vol. 18, No. 2, 2007, pp. 185–202. https://doi.org/10.1007/s11044-007-9084-0.

[23] Shabana, A. A., "Flexible Multibody Dynamics: Review of Past and Recent Developments," *Multibody System Dynamics*, Vol. 1, No. 2, 1997, pp. 189–222. https://doi.org/10.1023/A:1009773505418.

[24] Shabana, A. A., and Yakoub, R. Y., "Three Dimensional Absolute Nodal Coordinate Formulation for Beam Elements: Theory," *Journal of Mechanical Design*, Vol. 123, No. 4, 2001, pp. 606–613. https://doi.org/10.1115/1.1410100.

[25] Romero, I., "A comparison of finite elements for nonlinear beams: the absolute nodal coordinate and geometrically exact formulations," *Multibody System Dynamics*, Vol. 20, No. 1, 2008, pp. 51–68. https://doi.org/10.1007/s11044-008-9105-7.

[26] del Carre, A., and Palacios, R., "Simulation and Optimization of Takeoff Maneuvers of Very Flexible Aircraft," *Journal of Aircraft*, Vol. 57, No. 6, 2020, pp. 1097–1110. https://doi.org/10.2514/1.C035901.

[27] Palacios, R., and Cesnik, C. E. S., *Dynamics of Flexible Aircraft*, Cambridge University Press, 2023. https://doi.org/10.1017/9781108354868.

[28] Bauchau, O. A., *Flexible Multibody Dynamics*, Vol. 176, Springer, Dordrecht [u.a.], 2011.

[29] Düssler, S., and Palacios, R., "Enhanced Unsteady Vortex Lattice Aerodynamics for Nonlinear Flexible Aircraft Dynamic Simulation," *AIAA Journal*, Vol. 62, No. 3, 2024, pp. 1179–1194. https://doi.org/10.2514/1.J063174.

[30] Düssler, S., Goizueta, N., Muñoz-Simón, A., and Palacios, R., "Modelling and Numerical Enhancements on a UVLM for Nonlinear Aeroelastic Simulation," AIAA SCITECH 2022 Forum, 2022. https://doi.org/10.2514/6.2022-2455.

[31] Castrichini, A., "Parametric Assessment of a Folding Wing-Tip Device for Aircraft Loads Alleviation," Ph.D. thesis, University of Bristol, 2017.

[32] Muñoz-Simón, A., "Vortex-lattice-based nonlinear aeroservoelastic modelling and analysis of large floating wind turbines," Ph.D. thesis, Imperial College London, 2021. https://doi.org/10.25560/96986.

[33] Murua, J., Palacios, R., and Graham, J. M. R., "Applications of the unsteady vortex-lattice method in aircraft aeroelasticity and flight dynamics," *Progress in Aerospace Sciences*, Vol. 55, 2012, pp. 46–72. https://doi.org/10.1016/j.paerosci.2012.06.001.

[34] Artola, M., Goizueta, N., Wynn, A., and Palacios, R., "Proof of Concept for a Hardware-in-the-Loop Nonlinear Control Framework for Very Flexible Aircraft," *AIAA Scitech 2021 Forum*, American Institute of Aeronautics and Astronautics, Reston, Virginia, 2021. https://doi.org/10.2514/6.2021-1392.

Appendix. Verification of the Flexible Multibody Solution

To verify the nonlinear multibody formulation above we first study a slanted double pendulum. It will also demonstrate the accuracy and robustness of the proposed methodology. The above-mentioned flexible multibody formulation is implemented in SHARPy [20], an open-source, nonlinear aeroelastic simulation toolbox*. The common parameters of the three different models at baseline rigidity $\sigma = 1$ are tabulated in Table 3.

Table 3 Common model parameters for rigidity ratio $\sigma = 1$

Parameters	Description	Values	Units
l_x	Axial length	0.5	m
l_d	Cross-sectional side length	0.02	m
ρ	Material density	2700	kg m^{-3}
I_y	Moment of inertia w.r.t. y axis	1.127×10^{-2}	kg m
I_x	Moment of inertia w.r.t. x axis	3.600×10^{-5}	kg m
EA	Axial rigidity	2.800×10^{7}	kg m s^{-2}
GA	Shear rigidity	1.037×10^{7}	kg m s^{-2}
EI	Flexural rigidity	9.333×10^{2}	kg m^3 s^{-2}
GJ	Torsional rigidity	6.914×10^{2}	kg m^3 s^{-2}
g	Gravity	9.81	m s^{-2}

A. A rigid-body model

We have independently derived the analytical equations of motions for a flared rigid double pendulum under the influence of gravity, as shown in Figure 33, and implemented a solver in MATLAB. The flare angle β is defined as the clockwise angle of the positive y axis and the hinge axis, as shown in Figure 33a. The fold angles θ_1 and θ_2 are defined in Figure 33b, where the first pendulum rotates about the y axis. Note θ_2 is on the $x-z$ plane only when β is 0, otherwise it is an angle perpendicular to the hinge plane in the general 3D space.

For this rigid double pendulum, the locus of the second pendulum traces a cone, rotated by θ_1 about the y axis, exactly for any arbitrary β. Hence we arrive at analytical expressions for the locations of the center of mass of the two pendulums $\boldsymbol{r}_{1_{mid}}$ and $\boldsymbol{r}_{2_{mid}}$ as, assuming uniform properties,

*available at `https://github.com/ImperialCollegeLondon/sharpy`

$$\boldsymbol{r}_{1_{mid}} = \begin{bmatrix} x_{1_{mid}} \\ y_{1_{mid}} \\ z_{1_{mid}} \end{bmatrix} = \begin{bmatrix} l_1\cos(\theta_1)/2 \\ 0 \\ -l_1\sin(\theta_1)/2 \end{bmatrix}, \text{ and } \boldsymbol{r}_{2_{mid}} = \begin{bmatrix} x_{2_{mid}} \\ y_{2_{mid}} \\ z_{2_{mid}} \end{bmatrix} = \begin{bmatrix} 2x_{1_{mid}} + l_2 x_{2_{rot}}/2 \\ 2y_{1_{mid}} + l_2 y_{2_{rot}}/2 \\ 2z_{1_{mid}} + l_2 z_{2_{rot}}/2 \end{bmatrix}, \tag{13}$$

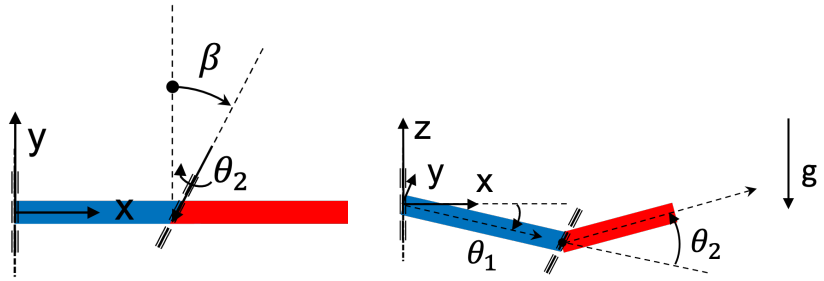
where

$$\begin{bmatrix} x_{2_{rot}} \\ y_{2_{rot}} \\ z_{2_{rot}} \end{bmatrix} = \begin{bmatrix} \cos(\theta_1) & 0 & \sin(\theta_1) \\ 0 & 1 & 0 \\ -\sin(\theta_1) & 0 & \cos(\theta_1) \end{bmatrix} \begin{bmatrix} \left(\sin(\beta)\sin(\beta) + \frac{\cos(\beta)(1+\cos(2\beta))}{\sqrt{2+2\cos(2\beta)}}\right)\cos(\theta_2) \\ \left(\sin(\beta)\cos(\beta) - \frac{\cos(\beta)\sin(2\beta)}{\sqrt{2+2\cos(2\beta)}}\right)\cos(\theta_2) \\ -\sin(\theta_2)\cos(\beta) \end{bmatrix} \tag{14}$$

in which the last term is the location of a point in Cartesian coordinates along the base of the cone by θ_2 with a half cone angle of $(\pi - \beta)$. The Lagrangian of the system is hence a function of the derivatives of $\boldsymbol{r}_{1_{mid}}$ and $\boldsymbol{r}_{2_{mid}}$, as well as other constants, expressed as

$$\begin{aligned} \mathcal{L} = &- (m_1 g z_{1_{mid}} + m_2 g z_{2_{mid}}) + \left(\frac{m_1}{2} \left| \frac{d\boldsymbol{r}_{1_{mid}}}{dt} \right|^2 + \frac{m_2}{2} \left| \frac{d\boldsymbol{r}_{2_{mid}}}{dt} \right|^2 \right. \\ &\left. + \frac{I_{1_y}}{2} \left| \frac{d\theta_1}{dt} \right|^2 + \frac{I_{2_y}}{2} \left| \cos(\beta) \frac{d\theta_2}{dt} + \frac{d\theta_1}{dt} \right|^2 + \frac{I_{2_x}}{2} \left| \sin(\beta) \frac{d\theta_2}{dt} \right|^2 \right) \end{aligned} \tag{15}$$

where the first term is the kinetic and the second potential energy. With Hamilton's principle we obtain the system of equations, which are marched in time with the Runge-Kutta solver in MATLAB.



(a) Top view at t=0 **(b) 3D view at t>0**

Fig. 33 Setup of the rigid-body model

B. Flexible model

A flexible double pendulum with a flared hinge as in Figure 33 was also created in MSC NASTRAN 2022.1. To model the slanted hinge, two CBUSH elements of sufficient stiffness ($1.00 \times 10^{12}\,\mathrm{kg\,m^{-1}\,s^{-2}}$) were placed, enforcing coincidence of two RBE2 elements, consisted of two pairs of GRID points, along the hinge line as described in Section II.A.3. NASTRAN SOL400 was used to perform nonlinear multibody analysis.

C. Results on a slanted double pendulum

Three cases ($\beta = 0, 45°, 90°$) are investigated, corresponding to three very different sets of dynamics in play. All cases are initialised with θ_{1_0} and θ_{2_0} at 0°. A simulation time of 2 seconds used, which is very close to the period of the pendulum motion. Correspondingly Δt for each of the MATLAB, MSC NASTRAN, and SHARPy model is 3.54×10^{-3} s, 2.00×10^{-4} s, and 2.00×10^{-3} s respectively. 5 elements are used with the SHARPy model, and 10 CBEAM elements with MSC NASTRAN. Note that NASTRAN CBEAM elements are 2-noded, whereas SHARPy beam elements are 3-noded.

Consider first $\beta = 0$. This is equivalent to the case when we have a planar double pendulum, and hence $y_{2_{tip}}$ is 0 throughout and are not shown in Figures 34a and b, where the tip position is plotted against time. As expected, the motion is entirely contained in the x-z plane, and deviations in the NASTRAN solution from the rigid MATLAB result are only evident after almost a period when chaotic effects are more prone to kicking in.

Next, we consider $\beta = 90°$, which is when it effectively becomes a single planar pendulum, a problem to which an analytical solution exists. As this is not computationally demanding, and also likely as the rotation about the axial direction have not caused numerical issues, we have not observed any meaningful deviation from the rigid result.

Finally, we consider $\beta = 45°$, in which the slanted double pendulum undergoes translation and rotation in the 3D space, as evidenced by the non-zero $y_{2_{tip}}$ values. The flexible (SHARPy and NASTRAN) results shows deviations from the rigid comparison during the second swing, when the elastic modes of the system is energised, supported by the fact that the flexible results are almost coincident.

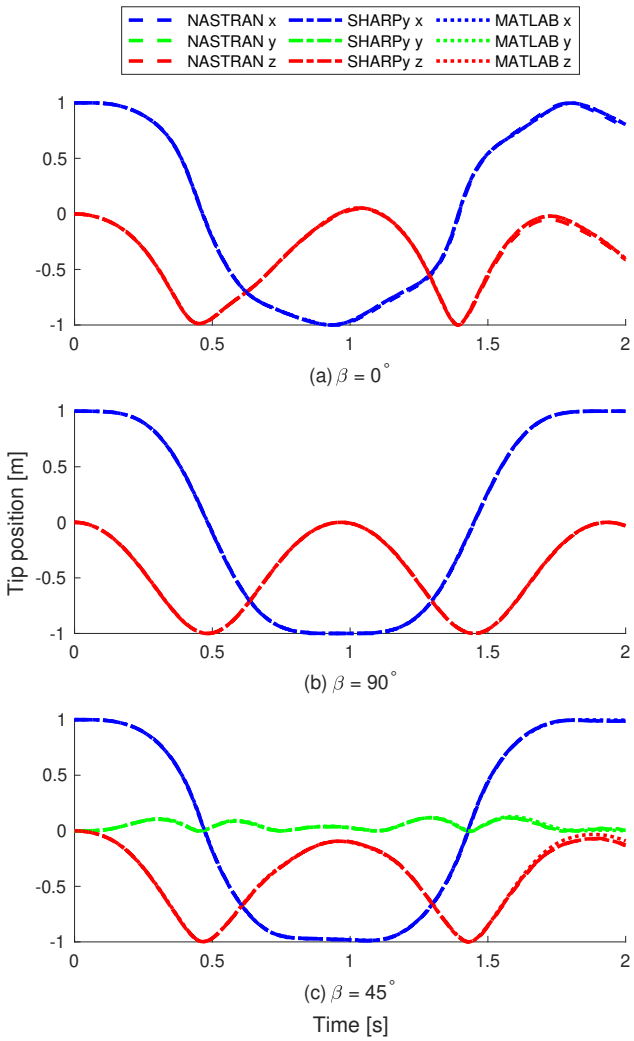


Fig. 34 $r_{2_{tip}}$ time histories for various β values, $\sigma = 1$

To further investigate the robustness of the SHARPy implementation we have reduced the stiffness constants by one-hundred-fold. Figure 35 demonstrates the accuracy of the predicted response at the tip. Here, the beam becomes very flexible and the rigid body motion at the hinge is progressively masked by the flexible deformations of the beams. These tests have established the validity and robustness of the SHARPy hinge condition across various stiffness regimes, geometry, and initial conditions. Additional cases for verification and comparison are available in the accompanying online repository.

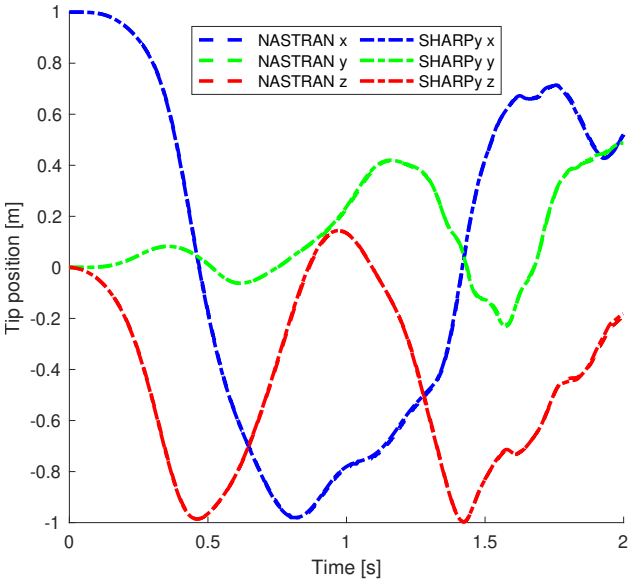


Fig. 35 $r_{2_{tip}}$ **time histories for** $\beta = 45$**,** $\sigma = 0.01$